Chronology and eccentricity phasing for the Early Turonian greenhouse (~93-94 Ma): constraints on astronomical control of the carbon cycle

Jiří Laurin[1], David Uličný[1], Stanislav Čech[2], Jakub Trubač[3], Jiří Zachariáš[3], and Andrea Svobodová[4]

[1]Academy of Sciences of the Czech Republic (ASCR)
[2]Czech Geological Survey
[3]Charles University
[4]Institute of Geology of the Czech Academy of Sciences

November 30, 2022

Abstract

The Early Turonian interval represents a unique confluence of climatic and oceanographic conditions including peak surface temperatures, high greenhouse-gas concentrations and maximum Phanerozoic sea level. The susceptibility of this climate mode to short-term forcings such as astronomically paced insolation remains poorly understood partly due to a limited time control and unknown phasing of astronomical cycles in this interval. Here we offer a refined astrochronology of the Early Turonian based on laterally consistent precession signals preserved in offshore strata of the Bohemian Cretaceous Basin (central Europe). Pristine amplitude modulation verified through interference patterns in depth-frequency plots provides a robust indication of ~100-kyr and 405-kyr eccentricity phases (maxima and minima) that are pinned to ammonite biozones and new carbon-isotope data from two cores. The Early Turonian is estimated as 885 ±46 thousand years (kyr) in duration, with the Cenomanian-Turonian boundary predating the nearest 405-kyr maximum by 81 ±32 kyr. The results support a possible link of the recovery from Oceanic Anoxic Event II to increasing magnitude of seasonal insolation extremes due to rising eccentricity on 405-kyr and million-year (Myr) time scales. Superimposed upon this trend are small-scale carbon-isotope anomalies the pacing of which passes from ~110 kyr, resembling short eccentricity, to ~170-kyr, possibly related to obliquity modulation. The loss of short-eccentricity pacing despite Myr-scale increase in eccentricity amplitudes suggests decoupling of the carbon-cycle perturbations from low-latitude seasonal insolation and involvement of mid- to high-latitude carbon reservoirs.

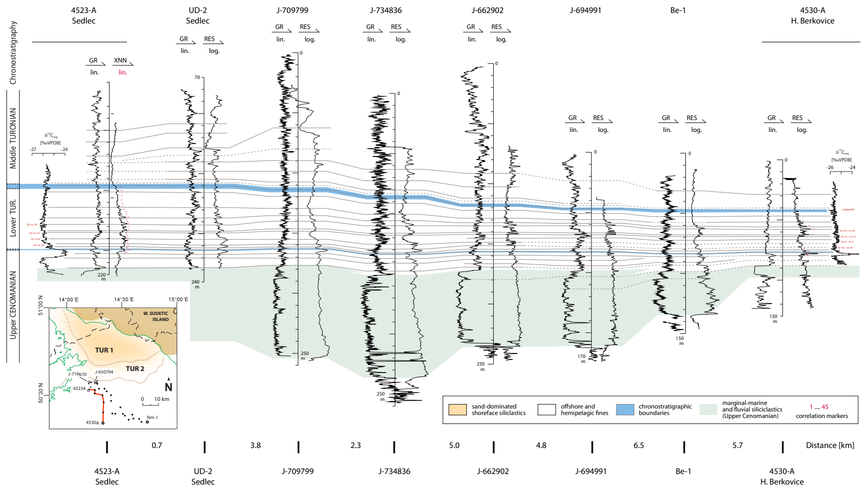

Figure S3. Well-log correlation of boreholes 4523-A and 4530-A.

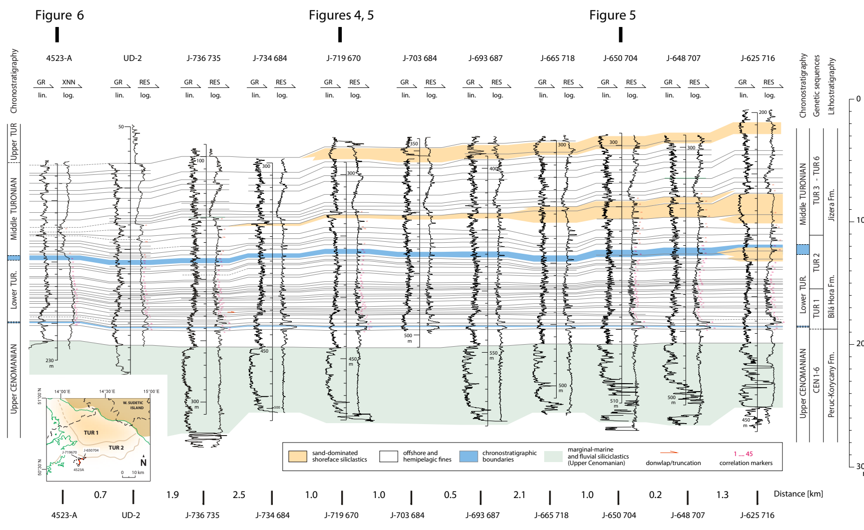

Figure S1. Well-log correlation of key boreholes discussed in this study.

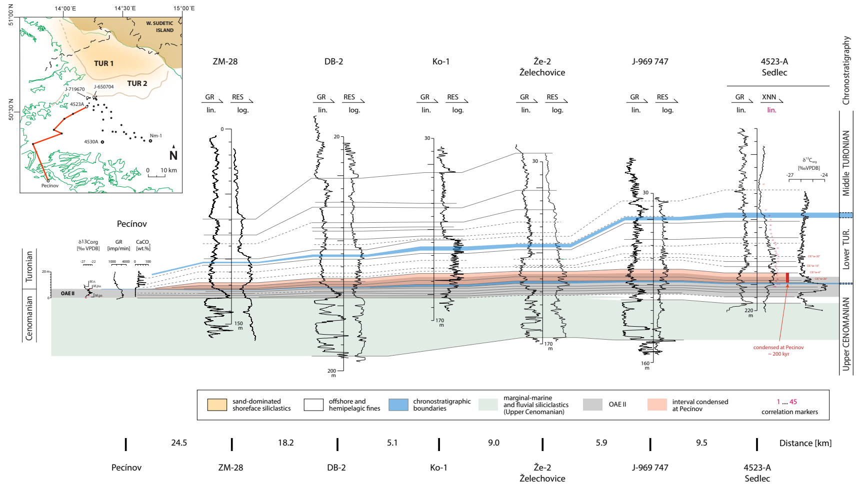

Figure S4. Well-log correlation of boreholes 4523-A and the Pecínov section. Pecínov data are adopted from Košťák et al. (2018).

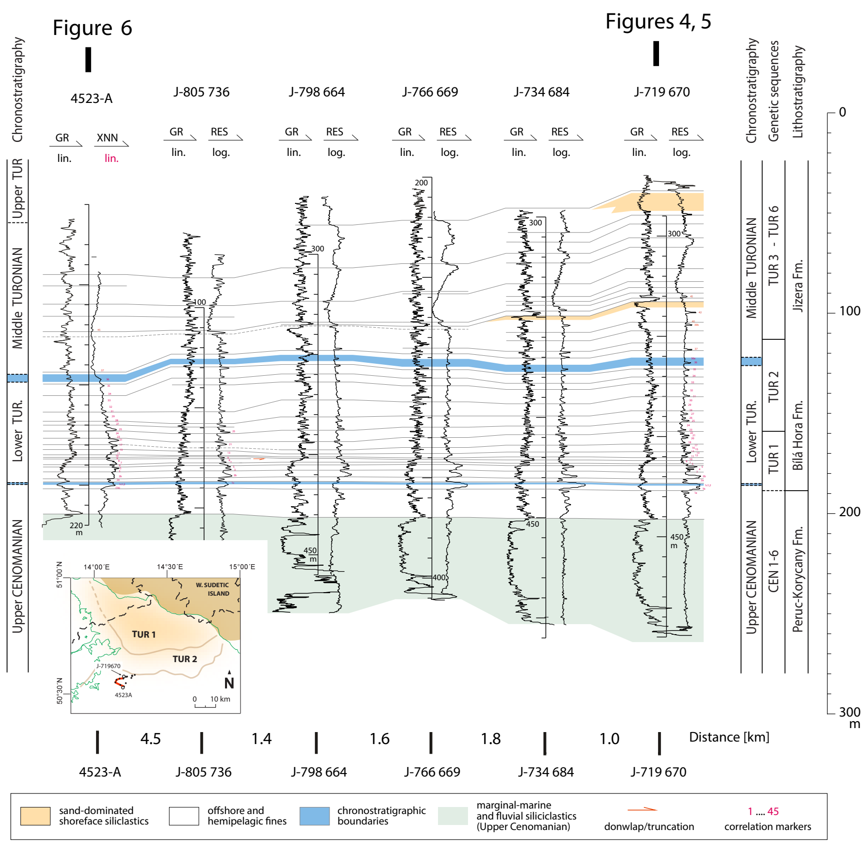

Figure S2. Well-log correlation of key boreholes discussed in this study.

Chronology and eccentricity phasing for the Early Turonian greenhouse (~93-94 Ma): constraints on astronomical control of the carbon cycle

Jiří Laurin[1], David Uličný[1], Stanislav Čech[2], Jakub Trubač[3], Jiří Zachariáš[3], Andrea Svobodová[4]

[1] Institute of Geophysics of the Czech Academy of Sciences, Boční II/1401, 141 31 Prague, Czech Republic

[2] Czech Geological Survey, Prague, Czech Republic

[3] Institute of Geochemistry, Mineralogy and Mineral Resources, Charles University, Prague, Czech Republic

[4] Institute of Geology of the Czech Academy of Sciences, Prague, Czech Republic

ABSTRACT

The Early Turonian interval represents a unique confluence of climatic and oceanographic conditions including peak surface temperatures, high greenhouse-gas concentrations and maximum Phanerozoic sea level. The susceptibility of this climate mode to short-term forcings such as astronomically paced insolation remains poorly understood partly due to a limited time control and unknown phasing of astronomical cycles in this interval. Here we offer a refined astrochronology of the Early Turonian based on laterally consistent precession signals preserved in offshore strata of the Bohemian Cretaceous Basin (central Europe). Pristine amplitude modulation verified through interference patterns in depth-frequency plots provides a robust indication of ~100-kyr and 405-kyr eccentricity phases (maxima and minima) that are pinned to ammonite biozones and new carbon-isotope data from two cores. The Early Turonian is estimated as 885 ±46 thousand years (kyr) in duration, with the Cenomanian-Turonian boundary predating the nearest 405-kyr maximum by 81 ±32 kyr. The results support a possible link of the recovery from Oceanic Anoxic Event II to increasing magnitude of seasonal insolation extremes due to rising eccentricity on 405-kyr and million-year (Myr) time scales. Superimposed upon this trend are small-scale carbon-isotope anomalies the pacing of which passes from ∼110 kyr, resembling short eccentricity, to ∼170-kyr, possibly related to obliquity modulation. The loss of short-eccentricity pacing despite Myr-scale increase in eccentricity amplitudes suggests decoupling of the carbon-cycle perturbations from low-latitude seasonal insolation and involvement of mid- to high-latitude carbon reservoirs.

1. INTRODUCTION

Following a major climatic perturbation related to the Oceanic Anoxic Event II (OAE II; Schlanger and Jenkyns, 1976), the Early Turonian, ~93-94 million years (Myr) ago, was an episode of stabilized climate of what is considered the peak Phanerozoic greenhouse warmth (Clarke and Jenkyns 1999; Friedrich et al. 2012). Both surface temperatures and global sea level reached extreme levels owing primarily to high rates of ocean-crust production and CO_2 outgassing (e.g., Jones and Jenkyns 2001). Compared to OAE II, the carbon-isotope signature is enriched in the isotope ^{12}C suggesting reduced capacity of oceanic and terrestrial organic reservoirs, i.e., improved recycling of organic carbon that likely contributed to radiative forcing of greenhouse gases. Short-term (10s kyr) carbon-isotope anomalies with magnitudes 0.2-0.5 ‰ in both organic and carbonate carbon (Jarvis et al. 2006, 2015; Fig. 1) point to transient perturbations to the carbon cycle of possible Milankovitch origin (Voigt et al. 2007). The Early Turonian thus represents a rare example of peak greenhouse climate, destabilized on short time scales by external forcings. The potential astronomical origin represents a testable hypothesis that can be evaluated with detailed temporal constraints.

Earlier astrochronologies suggested durations of the Early Turonian in the range of 0.78 to 0.84 Myr (Sageman et al. 2006; Voigt et al. 2008; Tab. 1), but a substantial (~20%) disagreement exists between these estimates and the duration provided by the Geological Time Scale 2012 (GTS2012; Gradstein et al. 2012). More recent studies (Sprovieri et al. 2013; Eldrett et al. 2015; Batenburg et al. 2016) provided detailed astronomical contexts including the phases of orbital eccentricity, but their chronostratigraphy remains controversial (Fig. 1; Tab. 1).

In order to test the published results and provide additional details that might help to better understand the temporal relationships, we present a new astrochronology based on well-preserved precessional and eccentricity signals in the Bohemian Cretaceous Basin. The results offer a robust interpretation of ~100-kyr, 405-kyr and ~2.4-Myr eccentricity phases that provide new insights into the role of astronomical forcing in carbon-cycle perturbations.

2. DEPOSITIONAL SETTING

The Bohemian Cretaceous Basin formed as a continental through shallow-marine siliciclastic system along reactivated, NW-trending faults of the Elbe fault zone (Fig. 2; Uličný et al. 2009). The Cenomanian-Turonian interval is characterized by a basinwide flooding and expansion of hemipelagic carbonates across the basin. The overlying Turonian statigraphy consists predominantly of coarse-grained progradational wedges of deltaic and nearshore siliciclastics (genetic sequences TUR1-3; Uličný et al. 2009) that interfinger distally with offshore to hemipelagic fines (Figs. S1-S6). Astronomical signals are best expressed in distal parts of the siliciclastic depocenter where hemipelagic marlstones and limestones (type A cycles; Figs. 3, S7 and S8) pass upward into offshore through distal prodelta facies with cyclic variations in sand vs. mud contents (highlighted by carbonate cementation; type B cycles; Figs. S7, S8).

3. DATA AND METHODS

3.1. Data

This study is based on subsurface data. An extensive borehole and well-log database provides a 3-dimensional stratigraphic framework (Uličný et al., 2009, 2014) and makes it possible to (i) trace changes in lithofacies and stratal geometries in the study area to determine the most suitable sites for time series analysis, and (ii) correlate biostratigraphic datums, carbon-isotope events and floating astrochronology across the basin (Figs. S1-S6).

All boreholes examined here exhibit long-term changes in sedimentation rate reflecting a long-term progradation of the marginal-marine siliciclastic system and shallowing of the coeval hemipelagic setting. Shorter-term fluctuations in sedimentation rates related to non-deposition and/or erosion across syndepositional faults are documented locally by angular relationships of well-log correlation markers (Figs. S1, S2). Boreholes suitable for time-series analysis and the construction of astronomical age model were selected from the prodeltaic zone based on two criteria: (i) The long-term change in sedimentation rate follows a simple pattern that can be modeled and removed numerically (e.g., linear change in sedimentation rate matched by a reciprocal function of signal wavelength in the depth-frequency plot; Fig. 4b). (ii) Short-term hiatuses and other fluctuations in sedimentation rates are absent or short relative to the tuning targets. The closest fit to these criteria is found in borehole J-719670 located ~5 km offshore from the progradational limit of sequence TUR2 (Fig. 2). Complementary analyses were executed on a series of other boreholes from the along-dip correlation profile. The list of key boreholes, their geographic coordinates and types of data are provided in Table S1.

Time-series analysis (section 3.4) was applied primarily to high-resolution resistivity logs that serve as a proxy for variations in sand/mud ratio and carbonate cementation. The LL7 focused laterolog probe offers a favorable combination of sensitivity to dm- to meter-scale lithological variations in the mixed carbonate-siliciclastic strata, and noise attenuation (gamma-ray logs appear excessively noisy at the dm to meter scales as revealed by comparing closely spaced boreholes). The depth resolution of digitized resistivity logs is 10 cm, which in the reference borehole J-719670 corresponds to a minimum of 10 samples per the shortest (precessional) cycle discussed in this paper.

Isolated core samples from two boreholes (J-703684 and J-854604) and complete cores from boreholes 4523-A Sedlec and 4530-A Horní Beřkovice (Fig. 3) were available for a detailed examination of lithology and geochemistry. Greyscale-density profiles for the 4523-A Sedlec core were extracted from high-resolution (~10 pixels/mm) photographs using the image-processing software ImageJ (National Institutes of Health, Bethesda, MD).

3.2. Geochemistry

Samples from the 4523-A Sedlec and 4530-A Horní Beřkovice cores were analyzed for carbon-isotope composition of bulk organic carbon ($\delta^{13}C_{org}$). The measurements were performed in the Stable Isotope Laboratory of the Geological Survey, Prague (4523-A), and the Institute of Geochemistry, Mineralogy and Mineral Resources, Charles University, Prague (4530-A). Samples (10-15 g) were pulverized to an analytical-grade powder and decalcified using 10% HCl. Additional details are provided in Text S1. Data are reported relative to the Vienna Peedee Belemnite (VPDB) standard. Reproducibility of duplicate measurements was 0.12 ±0.08 (1σ) ‰ VPDB. The temporal resolution of $\delta^{13}C_{org}$ data from the core 4523-A is 6.7 ±4.6 (1σ) kyr, according to the age model presented here.

Major and trace element concentrations were measured with an XRF spectrometer NITON XL3t GOLDD+; the XRF output was calibrated using 10 samples analyzed in an accredited laboratory of the Nanotechnology Centre, Technical University of Ostrava.

3.3. Chronostratigraphy, biostratigraphy

The Cenomanian/Turonian (C/T) boundary is constrained by a carbon-isotope correlation to the USGS #1 Portland core (Fig. S13) and well-log correlation of the base of ammonite Zone *Watinoceras devonense* from the Pecínov section, indicated there by the occurrence of inoceramid bivalve *Mytiloides puebloensis* (Fig. S4; cf. Košťák et al., 2018). The Lower Turonian ammonite Zone *Mammites nodosoides* is delineated by FO *M. nodosoides* at Pecínov (Košťák et al. 2018); a relatively large uncertainty in the correlation FO *M. nodosoides* and *W. devonense* to borehole 4523-A Sedlec (Fig. 3) is due to stratigraphic condensation at Pecínov (Figs. S4 and S13). The base of nannofossil Zone UC 7 which correlates above the base of the *M. nodosoides* Zone (Burnett 1998) is identified at approximately 178.75-181.75 m depth of the core 4523-A (Text S2). The first occurrence of the ammonite *Collignoniceras woollgari* (Mantell), which marks the Lower/Middle Turonian boundary (Gradstein et al. 2012), is correlated from borehole Nm-1 (Figs. S5, S6). The base of the Middle Turonian is further confirmed by the Lulworth carbon-isotope excursion (Jarvis et al. 2006; Fig. 1) identified in boreholes 4523-A and 4530-A (Fig. 3).

3.4. Time-series analysis and signal processing

Spectral estimates are calculated with the multitaper method (MTM; Thomson 1982) and evolutive harmonic analysis (EHA; Meyers et al. 2001). The statistical significance of the spectral results is quantified using the MTM harmonic F-test (Thomson 1982), and the assignment of spectral maxima to precessional, obliquity and eccentricity terms is verified with the Average Spectral Misfit (ASM; Meyers and Sageman 2007). Frequencies of orbital eccentricity for ASM analysis are estimated from the solutions La2010a through La2010d (Laskar et al. 2011a) following the approach of Malinverno et al. (2010) and Meyers et al. (2012b). Precessional and obliquity frequencies for ASM analysis are adopted from Waltham (2015). All ASM parameters are listed in Tables S2a and S2b. The TimeOpt method (Meyers 2015) is used to verify the correlation between the eccentricity signal and precessional envelope in selected intervals (Figs. S10, S11). All spectral estimates, ASM and TimeOpt calculations are conducted using the R package 'Astrochron', version 0.6 (Meyers, 2014; R Core Team, 2015). Signal filtering is performed with the Matlab script EPNOSE (Laurin et al. 2017) using a modification of the Taner filter (Taner 1992), which is symmetrical on a linear scale (Kodama and Hinnov 2014). Modulation envelopes were extracted with the Hilbert transform in the Matlab Signal Processing Toolbox; the algorithm is based on Marple (1999).

Data preparation included removal of a large-scale linear trend in sedimentation rate. This trend is manifested as a systematic drift in amplitude and F-test significance maxima approximating a reciprocal function of signal wavelength in the frequency domain (Figs. 4b and S9). To remove the linear trend, the depth scale of borehole J-719670 was modified by considering that the mean spatial period of the precessional cycle evolved linearly from 1/1.05 m at the depth of 403 m to 1/0.32 m at the depth of 368 m (Fig. 4b), and setting this path to a constant value of 1/1.05 m (Fig. 4c). An analogous adjustment is applied to borehole J-650704, where a linear change from the period of 1/1.01 m at the depth of 428 m to the period of 1/0.35 m at the depth of 395 m is tuned to a constant period of 1/1.01 m. The resulting vertical scales are referred to as "detrended depth scales" in this paper (Figs. 4 and 5). Importantly, this type of linear pre-tuning is applied to an interval the time span of which greatly exceeds the period of short-eccentricity cycles (>300 kyr) and therefore should not distort the ~100-kyr modulation patterns examined in this study (section 4.2; cf. Zeeden et al. 2015). In order to reduce variance in the carbonate-rich interval of type A cyclicity, resistivity logs were converted to their common logarithm prior to time-series analysis. Additional details are provided in sections 4.1 through 4.4.

3.5 Astronomical solutions

Precessional and eccentricity signatures identified in this study are compared primarily with the astronomical solution La2010d (Laskar et al. 2011a), because this solution provides the most recent estimate for the precessional index (note that later solutions – Laskar et al. 2011b; Zeebe 2017; Zeebe and Lourens 2019 – are limited to eccentricity). The La2010d reconstructions of precessional index and obliquity have been obtained following the procedure described in Wu et al. (2013). We note, however, that all solutions available to date are unreliable in their prediction of Myr-scale eccentricity modulation beyond ~55 Myr ago (Laskar et al. 2011b; Zeebe 2017; Zeebe and Lourens 2019). No attempt is therefore made in this study to pin the study interval to any particular segment of the astronomical solution. The La2010d series is used primarily as a constraint for the astronomical tuning target and its uncertainty. The solution La2004 (Laskar et al. 2004) is shown for comparison, because, unlike La2010d, it offers compatible eccentricity phases within the bounds of radioisotopic uncertainty (±0.15 Myr, Meyers et al. 2012a) and provides the closes fit to Myr-scale modulation in the Turonian interval (Ma et al. 2019).

3.6 Age model

Astrochronology is based on precessional and eccentricity signals identified in the study interval. To estimate the uncertainty related to unstable astronomical solutions, the interpreted precessional cycles are correlated to all segments of the solution La2010d (Laskar et al., 2011a) between 89 and 99 Myr ago that are compatible with eccentricity phasing in the study interval. Interpolation of the age-depth relationships is based on the Bayesian approach and executed with Bchron (Haslett and Parnell 2008). Further details are provided in section 4.4.

3.7 Terminology

The term "phasing" is used in this paper to refer to the timing of maxima and minima of astronomical signals. An attempt is made to distinguish the phasing of the original astronomical forcing from the phasing of filtered lithological or geochemical proxies of the astronomical forcing (through amplitude modulation and interference patterns of precessional signals).

In a previous study, Laurin et al. (2016) use the term frequency modulation (FM) to describe systematic changes in the frequency of astronomical signals in depth-frequency plots (EHA). Although the EHA patterns discussed here are analogous to Laurin et al.'s FM, a different term – interference patterns (IP) - is used here to avoid confusion with FM examined by other techniques (e.g., Liu et al. 1998; Hinnov 2000).

4. RESULTS

4.1. Astronomical signatures

Spectral estimates and interpretation of astronomical signatures focus on three reference boreholes: J-719670, J-650704, and 4523-A (see Methods; Fig. 3). Borehole J-719670 provides a well-preserved record for most of the Lower Turonian, and is therefore considered the primary reference section. Results for the lower and upper parts of the study interval are refined using data from boreholes 4523-A and J-650704.

4.1.1. Borehole J-719670, resistivity

Spectral estimates for a downhole resistivity log of this borehole show distinct power-spectral and F-test significance maxima in the astronomical band (Fig. 4). Power maxima exceeding the 90% significance level are labelled informally S_1 through S_4 and further discussed. A prominent cyclicity starts approximately 5 m beneath the C/T boundary, with most variance located in the frequency band ~0.25 cycle/m (~4 m period; S_2 in Fig. 4). Approximately 6 m above the C/T boundary, the S_2 signal starts fading and the variance is transferred to higher frequencies, namely S_4. This apparent increase in signal resolution follows decreasing carbonate contents and the onset of siliciclastic-dominated (type B) cyclicity that has a distinct response in the resistivity log. A refined, S_4-scale resolution for the C/T boundary interval is obtained from greyscale data from borehole 4523-A (section 4.1.3).

Further up-section, with an increase in siliciclastic contents related to progradation of sequence TUR2, the S_4 trace in EHA plot drifts to lower frequencies consistent with a linear increase in sedimentation rate (reciprocal function of signal wavelength). Removal of the trend (explained in section 3.4 and Fig. 4b) makes it possible to examine the detailed structure of the S_4 band; the signal is composed of two separate frequencies (labeled S_{4a} and S_{4b}) whose interference is coherent with the S_2 cyclicity (Figs. 4, 5). ASM analysis (Fig. 4d) suggests that the S_2 and S_4 signals correspond to cycles of orbital eccentricity (97-127 kyr; related to g_4-g_5 and g_4-g_2) and climatic precession (~19–23 kyr), respectively. The S_{4a} and S_{4b} components then correspond to the ~23-kyr (k+g_5 and k+g_2) and ~19-kyr (k+g_4 and k+g_3) terms of the precessional index, respectively (where k refers to Earth's precession rate, and g_2 through g_5 are the secular frequencies of planetary motion; Berger and Loutre 1990). A signature of axial obliquity (S_3) is relatively weak and localized; where present, its variance never exceeds variance of the precessional signal (variance ratio <0.7).

The EHA signatures (IP in Figs. 4 and 5) suggest well-preserved precessional and eccentricity signals throughout most of the Lower Turonian. Above the Lower/Middle Turonian boundary, however, the astronomical signals become less distinct at the J-719670 site. In addition, the lowermost Turonian of J-719670 exhibits minor condensation spanning marker bed 9 and corresponding to one S_4 (precessional) cycle (Fig. S1). To confirm and refine the estimate of astronomical cyclicity in these intervals, additional boreholes are examined.

4.1.2. Borehole J-650704, resistivity

This borehole is located approximately 4 km eastward of J-719670, closer to the main siliciclastic depocenter of the Turonian depositional system (Fig. 2). Proximity to the sediment source provides suitable conditions for the extension of the S_4 signal into the Middle Turonian (Fig. 3). Spectral estimates for the resistivity log reveal a pattern of S_2 and S_4 cyclicity, which is compatible with the results for borehole J-719670 (Fig. 5).

4.1.3. Borehole 4523-A, greyscale

Borehole 4523-A Sedlec is located down the depositional dip relative to boreholes J-719670 and J-650704 (Fig. 2). Type B cyclicity, which consists primarily of sand/mud alternations (Figs. S7, S8), is less well expressed in this distal area due to reduced textural variability and local winnowing. However, unlike resistivity logs of J-719670 and J-650704, the high-resolution greyscale record of 4323-A makes it possible to resolve the S_4 signal in carbonate-rich facies surrounding the C/T boundary (Fig. 6).

4.2. Eccentricity phasing

The initial information on the phasing of ~100-kyr and 405-kyr eccentricity cycles is obtained from bandpassed resistivity logs following removal of a linear trend in sedimentation rate (Fig. 5). The bandpassed proxy, however, does not bear any information on the polarity of the astronomical term. To estimate the phase of the filtered proxy relative to the phase of the eccentricity forcing, we employ a suit of additional indices including (i) amplitude modulation of bandpassed precessional signal (see section 4.2.1), and (ii) preservation of interference patterns of the precessional signals in depth-frequency plots. Details on the interpretation are given below.

4.2.1. Short eccentricity (~100-kyr)

The inherent role of orbital eccentricity (e) in the climatic impact of axial precession, quantified by the precessional index ($e \sin\omega$, where ω is the longitude of the perihelion from the moving equinox), results in an eccentricity-paced modulation of the amplitude of precessional signals (e.g., Berger and Loutre 1991). This amplitude modulation has therefore been acknowledged as a tool to identify eccentricity maxima and minima (e.g., Herbert 1992; Grippo et al. 2004; Zeebe et al. 2017; Laurin et al. 2017). Any signals filtered from geological data are, however, prone to distortion due to sedimentation-rate instabilities and introduction of noise (both natural and analytical) into the filtered bandwidth. An accurate extraction of amplitude-modulated signals from stratigraphic data involves additional challenges such as frequency leakage out of the filtered bandwidth or introduction of harmonic tones into the filtered bandwidth due to short-term fluctuations in accumulation rates, diagenesis or differential compaction. The use of amplitude modulation therefore requires additional support. Here, the integrity of the precessional envelope is evaluated using interference patterns in EHA plot, analogous to the evaluation of 400-kyr phase in a previous study (Laurin et al. 2016).

The composition of fundamental frequencies of the main terms of short-eccentricity (g_4-g_2 and g_4-g_5) and precessional index ($k+g_5$, $k+g_2$, $k+g_4$ and $k+g_3$; Berger and Loutre 1990) links the interference of precessional terms to the eccentricity phase, i.e., $(k+g_4)-(k+g_2) = g_4-g_2$, and $(k+g_4)-(k+g_5) = g_4-g_5$. As illustrated in Figure 5c, intervals of constructive interference of the ~19-kyr and ~23-kyr terms mark short-eccentricity maxima, and intervals of destructive interference are aligned with short-eccentricity minima. These patterns can be examined in EHA plots that also make it possible to identify non-stationarities and determine noise levels in the precessional band (see Laurin et al. 2016 for illustration of possible modes of signal distortion and their EHA signatures).

In the resistivity log of J-719670, the interference patterns are well preserved between correlation markers 10 and 37 (Fig. 4) suggesting that the precessional signal and its amplitude modulation are not severely distorted in this interval. The precessional envelope in J-719670 can also be extended some distance beneath a minor hiatus near marker bed 9. The J-650704 record is noisier, but exhibits interference patterns that are consistent with those in J-719670 (Fig. 5). The amplitude envelope of S_4 signal in J-719670 is therefore used in this study as the primary tool for the interpretation of short-eccentricity maxima and minima. For intervals lacking a robust precessional modulation, such as the Cenomanian/Turonian boundary interval, the short eccentricity phases are estimated from a filtered S_2 signal, the polarity of which is confirmed with the TimeOpt analysis (Figs. S10 and S11).

It should be noted that the above approach cannot resolve minor phase differences and deformations that are to be expected in this depositional setting. However, the method of astrochronological tuning applied here (section 4.4) is not sensitive to minor lead/lag differences in the precessional and eccentricity records; the phasing uncertainty is accommodated by the total uncertainty of the age model.

4.2.2. Long eccentricity (405-kyr)

The 405-kyr cycle, the rhythm of which is represented by signal S_1 (Fig. 4d), is part of the same astronomical forcing as the ~100-kyr eccentricity term. The preservation of its polarity should therefore be analogous to the preservation of short-eccentricity phasing inferred in section 4.2.1. This means that maxima in the filtered resistivity log should *approximate* the maxima in the original signal (as noted above, minor phase uncertainties are accommodated by the tuning approach). If so, then 405-kyr maxima should be located near marker beds 2a, 20 and 36 (Fig. 5). Support for this assumption can be sought in the modulation of precessional and short-eccentricity signals.

As with the short-eccentricity phasing, the phase of 405-kyr eccentricity (g_2-g_5) is involved in the interference of precessional terms. In this case, however, the interpretation in real stratigraphic data would require an exceptionally clear signal permitting separation of the 23.05-kyr ($k+g_5$) and ~21.81-kyr ($k+g_2$) precessional terms (Tab. S2a). In spite of an excellent signal preservation, these components cannot be resolved in the study interval. Other indices are therefore required.

Pronounced amplitude modulation and well-developed interference patterns in the precessional band can be expected to form preferably during 405-kyr maxima, as in the theoretical solutions. The nodes in 405-kyr eccentricity, in contrast, should exhibit relatively weak precessional signals and indistinct interference patterns in time-frequency plots (Fig. 5c). Following these assumptions, 405-kyr maxima should be centered between marker beds 17 – 21 and near markers 36 – 37, in agreement with the S_1 bandpass (Fig. 5a,b). This interpretation is further supported by a transient record of eccentricity in the Lower/Middle Turonian boundary interval in borehole Bch-1 (central part of the basin; Figs. 7a and S12).

Modulation of the short-eccentricity signal (S_2) is of limited use due to an upward decline in its power. Gradual facies change above marker bed 2b (Fig. S7) and local winnowing of marker bed 9 (Fig. 5) also corrupt the S_1 bandpass in the lower part of the study interval. To preserve a realistic, ~1:4 bundling of short-eccentricity vs. long-eccentricity cycles, the lowermost maximum of the 405-kyr eccentricity should be located some distance above the lowermost maximum of the S_1 bandpass, between markers 2b and 3 (between short-eccentricity maxima ecc2 and ecc3; Figs. 5 and 7).

The final support for the interpretation of 405-kyr phase comes from bundling ratios of short-eccentricity vs. precessional cycles that are controlled chiefly by changes in the instantaneous period of short-eccentricity cycles. The 405-kyr minima are typically associated with low instantaneous periods (as low as 77 kyr; Hinnov 2000) and low bundling ratios (as low as 1:3 during ~2.4-Myr nodes). In the study interval, the bundling ratios range from 3.5 to 5.7 with minima near marker beds 7 and 31, coincident with 405-kyr minima predicted by the S_1 bandpass and precessional interference patterns (Fig. 7).

4.3. Myr-scale eccentricity

The ~2.4-Myr modulation of orbital eccentricity related to the precession of perihelia of Earth and Mars ($g_4 - g_3$; Laskar et al. 2004) cannot be interpreted directly due to a relatively short time span of the study interval (~1 Myr). However, since long-term eccentricity minima exhibit suppressed ~100-kyr modulations (Fig. 5c; cf. Hinnov 2000), the exquisite preservation of ~100-kyr interference patterns in the middle part of the Lower Turonian and lower part of the Middle Turonian makes it possible to infer a broadly defined ~2.4-Myr maximum in this interval. Such a phasing implies a ~2.4-Myr node overlapping with OAE II, in agreement with the results of previous studies (Batenburg et al. 2016; Laurin et al. 2016; Ma et al. 2019).

4.4 Age model

The study interval spans twelve short-eccentricity cycles labelled ecc1 through ecc11 (a minor cycle at 405-kyr minimum is labelled ecc3b; Fig. 7). These cycles, combined with the precessional cyclicity, provide the basis for the construction of floating age model. The key issue affecting accuracy of the age estimate is the selection of tuning targets for the eccentricity and precessional signals. A constant tuning target, e.g., 95 kyr for short eccentricity, can be considered inaccurate, because the instantaneous period of this cycle varies significantly in the course of 405-kyr and Myr-scale modulations (e.g., Hinnov 2000). Tuning to a particular segment of an astronomical solution would settle this issue, but all astronomical solutions available to date are unreliable in their prediction of Myr-scale eccentricity modulation beyond ~55 Myr ago (Laskar et al. 2011a,b; Zeebe 2017; Zeebe and Lourens 2019). To estimate the uncertainty associated with Myr-scale modulation, we select a 10-Myr interval of the solution La2010d centered at 94 Myr ago (~C/T boundary) and tune the observed signals to every compatible segment of the theoretical solution in this interval.

The tuning is performed by linking individual S_4 cycles with precessional cycles of the La2010d solution (Laskar et al. 2011a) within the framework of

~100-kyr (S_2) and 405-kyr (S_1) maxima and minima interpreted in section 4.2. In this concept, the precessional cycles provide the temporal resolution and eccentricity cycles provide stability (by, for example, identifying missing precessional beats at eccentricity minima). Each tuning assigns floating ages to correlation markers 1 through 43, which are manifestations of the precessional (S_4) cyclicity (Figs. S14 and S15). The mean and standard deviation of the floating ages, calculated from the total number of tuned segments (n=21), constitute the nominal age model and uncertainty of the tuning target (Tab. S3).

An interpolation of the nominal age model to chronostratigraphic boundaries using the Bayesian approach (Bchron; Haslett and Parnell 2008) suggests an 885 kyr duration for the Early Turonian. The uncertainty of this time span is estimated as ±46 kyr (95% confidence interval) by combining the uncertainty of the location of chronostratigraphic boundaries (Fig. 3) and the uncertainty of the La2010d tuning target (Tab. 2). The age model makes it possible to define the mean floating ages and uncertainties for the ~100-kyr and 405-kyr maxima and minima (Fig. 8): the Cenomanian/Turonian boundary predates the nearest 405-kyr maximum by 81 ±32 kyr, and the Lower/Middle Turonian boundary coincides with another 405-kyr maximum within the uncertainty of ±33 kyr.

4.5 Age-calibrated $\delta^{13}C$

The Bayesian interpolation is further applied to estimate floating ages of carbon-isotope samples in borehole 4523-A (Fig. 8). This age calibration suggests that the negative shift in $\delta^{13}C$ following OAE II is superimposed upon increasing 405-kyr eccentricity. The temporal distribution of small-scale anomalies approximates a ~110-kyr pacing in the lowermost Turonian, but passes to a longer, ~170-kyr pattern towards the Middle Turonian (Fig. 8d).

5. DISCUSSION

5.1 Chronology of the Early Turonian

The floating-age estimate presented here falls within the range presented in previous studies (Tab. 1). It is most closely compatible with astrochronology of the Wunstorf core (Voigt et al. 2008), with which it shares the precession-scale resolution. The minor difference in the duration of Early Turonian (~40 kyr) between these models might be related to the selection of monochromatic precessional tuning target (21 kyr) and the loss of precessional signal in the uppermost part of the Lower Turonian at Wunstorf. Another robust estimate, the Portland time scale of Meyers et al. (2001, 2012a) and Sageman et al. (2006), appears ~100 kyr short compared to the Bohemian model. The difference is again possibly related to the use of a monochromatic tuning target, in this case the 95 kyr for short eccentricity in Portland (note that the use of mean short-eccentricity period of 110 kyr would increase the duration estimate by 16%, matching the Bohemian estimate within its uncertainty). Other published astrochronologies are difficult to assess due uncertainties in the definition of chronostratigraphic boundaries in the Bottaccione (Sprovieri et al. 2013), Contessa (Batenburg et al. 2016) and Iona (Eldrett et al. 2015) records.

5.2 Eccentricity phasing across OAE II

The inferred ~2.4-Myr node in eccentricity modulation during OAE II and a long-term increase in the eccentricity amplitudes towards the Middle Turonian are in agreement with previous results supporting the role of increasing seasonality in the recovery from OAE II (Batenburg et al. 2016; Laurin et al. 2016). The 405-kyr phasing, in contrast, cannot be compared directly with previous studies due to uncertainties in stratigraphic correlation to published sections (Figs. 1 and S17) and a lack of direct phase constraints across OAE II. Well-preserved astronomical signals allowing a robust interpretation of the 405-kyr phases have been described from the pre-OAE II interval at Furlo (Batenburg et al. 2016; Laurin et al. 2016). When extrapolating eccentricity cycles of the Bohemian record to the base of OAE II using published astrochronologies (Sageman et al. 2006; Ma et al. 2014; Fig. S13), the 405-kyr maxima appear ~90 kyr (80°) out-of-phase relative to the Furlo record (Fig. 8c). Considering that both the Early Turonian and pre-OAE II eccentricity records are robust, the most likely source of error is in the extrapolation across OAE II. Possible explanations of the misfit include non-deposition or condensation near the base of Livello Bonarelli at Furlo, or a minor underestimation of the period of the eccentricity tuning target in the OAE II chronology (since the 95 kyr target used in the Portland astrochronology is at the low range of eccentricity periods; see also section 5.1).

Another apparent misfit is found in the Early Turonian, when comparing the Bohemian 405-kyr record with eccentricity maxima inferred for the Contessa section (Batenburg et al. 2016; Figs. 1f and S17). The two records can, however, be aligned with each other when considering a ±150 kyr uncertainty for the Contessa section (Batenburg et al. 2016) and delineating the Cenomanian/Turonian boundary as in Wendler (2013) (Fig. S17).

5.3 Short-term $\delta^{13}C$ anomalies: interbasinal correlation

To facilitate the comparison of different records, we offer a simple adjustment of the English Chalk and Portland $\delta^{13}C$ curves based on linear interpolation between the C/T boundary and the newly proposed floating age of the Lower/Middle Turonian boundary (Fig. 8). This simplified approach suggests that the Holywell CIE (Jarvis et al. 2006) postdates the C/T boundary by 300-400 kyr and might be correlative to the excursion Tu2 or a minor anomaly above Tu1 at Wunstorf (supported by the first occurrence of *M. nodosoides* immediately above Tu2; Fig. 8; cf. Voigt et al. 2008). In the Bohemian Cretaceous Basin, the most likely candidate for the Holywell CIE is the excursion "se-10".

In general, a correlation of small-scale CIEs that lack a distinct structure or magnitude will remain ambiguous without biostratigraphic constraints or detailed age calibration of both the reference section and the correlated section. The original depth-domain profiles and time-domain profiles interpolated across large intervals can provide misleading information about the relative spacing of CIEs due to unrecognized changes in sedimentation rates and distorted age-depth relationships.

5.4 Short-term $\delta^{13}C$ anomalies: timing and origin

The ~100-kyr recurrence interval of short-term $\delta^{13}C$ anomalies in the earliest Turonian (Fig. 8) points to the possible influence of eccentricity-modulated seasonal insolation intensities on the carbon-cycle budget (cf. Berger et al. 1993). The $\delta^{13}C$ signature is, however, not strictly coherent with inferred short-eccentricity cycles (Fig. 6) suggesting a causal mechanism different from that proposed for other greenhouse intervals, e.g., Paleocene-Eocene (Cramer et al. 2003; Zeebe et al. 2017). The observed incoherency may point to the heterogeneous composition of carbon sources and sinks, involving sensitivity to different aspects of the insolation control (e.g., seasonal intensity vs. integrated seasonal insolation) and geographic locations. The possible role of high- or mid-latitude carbon reservoirs responding to meridional insolation gradients (cf. Raymo and Nisancioglu 2003) or integrated summer insolation (cf. Huybers 2006) is apparent in the transition towards ~170-kyr pacing of $\delta^{13}C$ anomalies in the mid Early Turonian (Fig. 8d). The ~170-kyr term occurs in amplitude modulation of axial obliquity (Hinnov 2000; Fig. S16) and its record in the isotopic balance of the carbon cycle can be amplified by the ~100-kyr residence time of carbon (Kump and Arthur 1999), analogous to the amplification of eccentricity terms from precessional modulation (e.g., Short et al. 1991; Herbert 1997).

Notably, the transition from short-eccentricity pacing to ~170-kyr pacing is superimposed upon the rising phase of long-term eccentricity modulation (Figs. 5 and 8b). The loss of eccentricity pacing of $\delta^{13}C$ excursions can therefore not be attributed to the inherent change in eccentricity amplitudes. To produce the observed pattern, the carbon-cycle perturbations must have decoupled from low-latitude seasonal insolation involving carbon storage in the monsoonal belt (cf. Rossignol-Stricks 1983). The lead control on carbon-isotope mass balance was transferred to mid- to high-latitudes during this interval, paralleling a Myr-scale, obliquity-paced carbon exchange inferred in previous studies (Wendler et al. 2014; Laurin et al. 2015) and the onset of long-term cooling of surface temperatures (cf. Pucéat et al. 2003; Friedrich et al. 2012).

SUMMARY

1. The record of precessional and eccentricity cycles in the Bohemian Cretaceous Basin constrains the duration of Early Turonian to 885 ±46 kyr.
2. The Cenomanian/Turonian boundary precedes the nearest 405-kyr maximum by 81 ±32 kyr. The recovery from OAE II is superimposed upon rising phases of 405-kyr and ~2.4-Myr eccentricity. The ~2.4-Myr cycle peaks between late Early Turonian and early Middle Turonian.
3. Astronomical control on the post-OAE II carbon cycle is documented by ~110-kyr pacing of $\delta^{13}C$ anomalies, which gives way to ~170-kyr obliquity pattern during the mid Early Turonian. The transition suggests decoupling of the carbon-cycle mass balance from low-latitude seasonal insolation and increasing role of high latitude carbon reservoirs.
4. The temporal and phasing constraints presented in this study can facilitate evaluation of short-term climate controls during peak greenhouse conditions.

ACKNOWLEDGMENTS

This research was supported by the Czech Science Foundation (GAČR) project No. 17-10982S, research program RVO 67985530 of the Czech Academy of Sciences of the Czech Republic, and research program RVO 67985831 of the Czech Geological Survey. Acquisition of digital well-log data and core samples was made possible through cooperation with DIAMO, s.p. and the Czech Geological Survey. We are particularly grateful for help with data acquisition to Roland Nádaskay, Jaroslav Valečka, Pavel Veselý, and Dana Čápová. Lukáš Hronec assisted with core preparation and sampling. Comments by Silke Voigt, David De

Vleeschouwer, and an anonymous reviewer helped considerably to improve the first version of this paper.

DATA AVAILABILITY

Data discussed in this paper are provided in the Supplementary Information, Datasets S1 through S5. By the time this article is accepted for publication, all data will be deposited in the Pangaea Data Publisher.

REFERENCES

Batenburg, S. J., D. De Vleeschouwer, M. Sprovieri, F. J. Hilgen, A. S. Gale, B. S. Singer, C. Koeberl, R. Coccioni, P. Claeys, and A. Montanari (2016), Orbital control on the timing of oceanic anoxia in the Late Cretaceous. Clim. Past, 12, 1995-2009, doi:10.5194/cp-12-1995-2016.

Berger, A.., and M. F. Loutre (1990), Origine des fréquences des éléments astronomiques intervenant dans le calcul de l'insolation. Bulletin de la Classe des sciences, tome 1. pp. 45-106, doi:10.3406/barb.1990.38523

Berger, A., and M. F. Loutre (1991), Insolation values for the climate of the last 10 million years, Quat. Sci. Rev. 10, 297–317.

Berger, A., M. F. Loutre, and C. Tricot (1993), Insolation and Earth's orbital periods. Journal of Geophysical Research, 98 (D6), 10,341–10,362, doi:10.1029/93JD00222.

Burnett, J.A. (1998), Upper Cretaceous. In: Calcareous Nannofossil Biostratigraphy (P.R. Bown), 132–199. British Micropalaeontological Society, London.

Čech, S., V. Klein, J. Kříž, and J. Valečka (1980), Revision of the Upper Cretaceous stratigraphy of the Bohemian Cretaceous Basin, Věst. Ústřed. Úst. Geol. (Bull. Geol. Surv. Prague), 55, 277–296.

Clarke, L. J., and H. C. Jenkyns (1999), New oxygen isotope evidence for long-term Cretaceous climatic change in the Southern Hemisphere, Geology, 27, 699–702, doi:10.1130/0091-7613(1999)027<0699:NOIEFL>2.3.CO;2.

Cramer, B. S., J. D. Wright, D. V. Kent, and M. P. Aubry (2003), Orbital climate forcing of $\delta^{13}C$ excursions in the late Paleocene–early Eocene (chrons C24n–C25n), Paleoceanography, 18, 1097, doi:10.1029/2003PA000909.

Du Vivier, A. D. C., D. Selby, B. B. Sageman, I. Jarvis, D. R. Gröcke, and S. Voigt, S. (2014), Marine $^{187}Os/^{188}Os$ isotope stratigraphy reveals the interaction of volcanism and ocean circulation during Oceanic Anoxic Event 2, Earth Planet. Sc. Lett., 389, 23-33, doi:10.1016/j.epsl.2013.12.024.

Eldrett, J.S., Ma, C., Bergman, S.C., Lutz, B., Gregory, F.J., Dodsworth, P., Phipps, M., Hardas, P., Minisini, D., Ozkan, A., Ramezani, J., Bowring, S.A., Kamo, S.L., Ferguson, K., Macaulay, C., and Kelly, A.E. (2015), An astronomically calibrated stratigraphy of the Cenomanian, Turonian and earliest Coniacian from the Cretaceous Western Interior Seaway, USA: Im- plications for global chronostratigraphy. Cretaceous Research, v. 56, p. 316–344, https://doi.org/10.1016/j.cretres.2015.04.010.

Friedrich, O., R. D. Norris, and J. Erbacher (2012), Evolution of middle to Late Cretaceous oceans—A 55 m.y. record of Earth's temperature and carbon cycle, Geology, 40, 107–110, doi:10.1130/G32701.1.

Gradstein, F.M., Ogg, J.G., Schmitz, M. and Ogg, G. (2012), The Geologic Time Scale: Elsevier, 1144 p.

Grippo, A., Fischer, A.G., Hinnov, L.A., Herbert, T.D., Premoli Silva, I. (2004), Cyclostratigraphy and chronolo- gy of the Albian stage (Piobbico Italy). In: D'Argenio, B. et al. (Eds.), Cyclostratigraphy: Approaches and Case Histories. Special Publication SEPM (Society for Sedi- mentary Geology) 81, 57–81.

Hinnov, L.A. (2000), New perspectives on orbitally forced stratigraphy: Annual Review of Earth and Planetary Sciences, 28, 419–475.

Haslett, J., & Parnell, A. (2008), A simple monotone process with application to radiocarbon-dated depth chronologies. Journal of the Royal Statistical Society: Series C (Applied Statistics), 57(4), 399–418.

Hay, W. W., R. M. DeConto, C. N. Wold, K. M. Wilson, S. Voigt, M. Schulz, A. Wold-Rossby, W.-C. Dullo, A. B. Ronov, A. N. Balukhovsky, and E. Söding (1999), Alternative global Cretaceous paleogeography, in Evolution of the Cretaceous Ocean-Climate System, Geol. Soc. Am. Special Paper 332, edited by E. Barrera and C. C. Johnson, 1-47, Boulder, Colorado.

Herbert, T.D. (1992), Paleomagnetic calibration of Milankovitch cyclicity in Lower Cretaceous sediments. Earth. Planet. Sci. Lett,. 112, 15–28.

Herbert, T. D. (1997), A long marine history of carbon cycle modulation by orbital-climatic changes. Proceedings of the National Academy of Sciences of the United States of America, 94(16), 8362–8369. doi: 10.1073/pnas.94.16.8362

Huybers, P. J. (2006), Early Pleistocene glacial cycles and the integrated summer insolation forcing, Science, 313, 508–511, doi:10.1126/ science.1125249.

Jones, C.E., and Jenkyns, H.C. (2001), Seawater strontium isotopes, Oceanic Anoxic Events, and seafloor hydrothermal activity in the Jurassic and Cretaceous. American Journal of Science, 301, 112–149.

Joo, Y. J., and B. B. Sageman (2014), Cenomanian to Campanian carbon isotope chemostratigraphy from the Western Interior Basin, U.S.A., J. Sediment. Res., 84, 529-542, doi:10.2110/jsr.2014.38.

Jarvis, I., A. S. Gale, H. C. Jenkyns, and M. A. Pearce (2006), Secular variation in Late Cretaceous carbon isotopes and sea-level change: evidence from a new d13C carbonate reference curve for the Cenomanian – Campanian (99.6 – 70.6 Ma), Geol. Mag., 143, 561–608.

Jarvis, I., J. Trabucho-Alexandre, D. R. Gröcke, D. Uličný, and J. Laurin (2015), Intercontinental correlation of organic carbon and carbonate stable isotope records: evidence of climate and sea-level change during the Turonian (Cretaceous), The Depositional Record, 1, 53-90, doi:10.1002/dep2.6.

Kodama, K. P., and Hinnov, L. A. (2014), Rock magnetic cyclostratigraphy. Oxford, UK: Wiley-Blackwell. https://doi.org/10.1002/9781118561294

Košťák, M., Čech, S., Uličný, D., Sklenář, J., Ekrt, B., and Mazuch, M. (2018), Ammonites, inoceramids and stable carbon isotopes of the CenomanianeTuronian OAE2 interval in central Europe: Pecínov quarry, Bohemian Cretaceous Basin (Czech Republic). Cretaceous Research, 87, 150-173.

Kump, L. R., and M. A. Arthur (1999), Interpreting carbon–isotope excursions: Carbonate and organic matter, Chem. Geol., 161, 181–198, doi:10.1016/S0009-2541(99)00086-8.

Laskar, J., P. Robutel, F. Joutel, M. Gastineau, A.C.M. Correia, and B. Levrard (2004), A long-term numerical solution for the insolation quantities of the Earth, Astron. Astrophys., 428, 261–285, doi:10.1051/0004-6361:20041335.

Laskar, J., Fienga, A., Gastineau, M., and Manche, H. (2011a), La2010: A new orbital solution for the long term motion of the Earth: Astronomy and Astrophysics, 532, A89, doi:10.1051/0004-6361/201116836.

Laskar, J., Gastineau, M., Delisle, J-B., Farrés, A., and Fienga, A. (2011b), Strong chaos induced by close encounters with Ceres and Vesta: Astronomy and Astrophysics, 532, L4, doi: 10.1051/0004-6361/201117504.

Laurin, J., Meyers, S.R., Galeotti, S., and Lanci, L. (2016), Frequency modulation reveals the phasing of orbital eccentricity during Cretaceous Oceanic Anoxic Event II and the Eocene hyperthermals. Earth and Planetary Science Letters, 442, 143-156, doi:10.1016/j.epsl.2016.02.047.

Laurin, J., S. R. Meyers, D. Uličný, I. Jarvis, and B. B. Sageman (2015), Axial obliquity control on the greenhouse carbon budget through middle- to high-latitude reservoirs, Paleoceanography, 30, 133-149, doi:10.1002/2014PA002736

Laurin, J., Růžek, B., and Giorgioni, M. (2017), Orbital signals in carbon isotopes: phase distortion as a signature of the carbon cycle. Paleoceanography, 32, 1236–1255. doi: 10.1002/2017PA003143

Liu, H.S. (1998), Glacial-interglacial changes induced by pulse modulation of the incoming solar radiation. J. Geophys. Res. 103(D20), 26147–26164.

Ma, C., S. R. Meyers, B. B. Sageman, B. S. Singer, and B. R. Jicha (2014), Testing the astronomical time scale for oceanic anoxic event 2, and its extension into Cenomanian strata of the Western Interior Basin (USA), Geol. Soc. Am. Bul., 126, 974-989.

Ma, C., Meyers, S.R., and Sageman, B.B. (2019), Testing Late Cretaceous astronomical solutions in a 15 million year astrochronologic record from North America. Earth and Planetary Science Letters, 513, 1-11.

Malinverno, A., E. Erba, and T. Herbert (2010), Orbital tuning as an inverse problem: Chronology of the early Aptian oceanic anoxic event 1a (Selli

Level) in the Cismon APTICORE, Paleoceanography, 25, PA2203, doi:10.1029/2009PA001769.

Marple, S. L. (1999), Computing the discrete-time analytic signal via FFT. IEEE Transactions on Signal Processing, 47(9), 2600–2603, doi:10.1109/78.782222.

Meyers, S. R. (2014), astrochron: An R Package for Astrochronology (Version 0.3.1). http://www.geology.wisc.edu/~smeyers.

Meyers, S.R. (2015), The evaluation of eccentricity-related amplitude modulation and bundling in paleoclimate data: An inverse approach for astrochronologic testing and time scale optimization: Paleoceanography, 30, doi:10.1002/2015PA002850.

Meyers, S. R., S. E. Siewert, B. S. Singer, B. B. Sageman, D. J. Condon, J. D. Obradovich, B. R. Jicha, and D. A. Sawyer (2012a), Intercalibration of radioisotopic and astrochronologic time scales for the Cenomanian-Turonian boundary interval, Western Interior Basin, USA, Geology, 40, 7-10, doi:10.1130/G32261.1.

Meyers, S. R., B. B. Sageman, and M. A. Arthur (2012b), Obliquity forcing of organic matter accumulation during Oceanic Anoxic Event 2, Paleoceanography, 27, PA3212, doi:10.1029/2012PA002286.

Meyers, S.R., Sageman, B.B., and Hinnov, L.A. (2001), Integrated quantitative stratigraphy of the Cenomanian-Turonian Bridge Creek Limestone Member using evolutive harmonic analysis and stratigraphic modeling: Journal of Sedimentary Research, 71, 628-644.

Meyers, S.R., and Sageman, B.B. (2007), Quantification of deep-time orbital forcing by average spectral misfit: American Journal of Science, 307, 773–792, doi:10.2475/05.2007.01.

Pearce, M.A., Jarvis, I., Ball, P.J., and Laurin, J. (2020), Palynology of the Cenomanian to lowermost Campanian (Upper Cretaceous) Chalk of the Trunch Borehole (Norfolk, UK) and a new dinoflagellate cyst bioevent stratigraphy for NW Europe. Review of Palaeobotany and Palynology, 278, 104188, doi:10.1016/j.revpalbo.2020.104188.

Pucéat, E., C. Lecuyer, S. M. F. Sheppard, G. Dromart, S. Reboulet, and P. Grandjean (2003), Thermal evolution of Cretaceous Tethyan marine waters inferred from oxygen isotope composition of fish tooth enamels, Paleoceanography, 18 (2), 1029, doi:10.1029/2002PA000823.

Raymo, M. E., and K. Nisancioglu (2003), The 41 kyr world: Milankovitch's other unsolved mystery, Paleoceanography, 18(1), 1011, doi:10.1029/2002PA000791.

R Core Team (2015), R: A language and environment for statistical computing. R Foundation for Statistical Computing, Vienna, Austria. http://www.R-project.org/.

Rossignol-Strick, M. (1983), African monsoons, an immediate climate response to orbital insolation. Nature 304, 46–49.

Sageman, B. B., S. R. Meyers, and M. A. Arthur (2006), Orbital time scale and new C-isotope record for Cenomanian-Turonian boundary stratotype, Geology, 34, 125-125.

Schlanger, S., Jenkyns, H. (1976). Cretaceous oceanic anoxic events: causes and consequences. Geol. Mijnb. 55, 179–184.

Short, D. A., J. G. Mengel, T. J. Crowley, W. T. Hyde, and G. R. North (1991), Filtering of Milankovitch cycles by Earth's geography, Quat. Res., 35, 157–173, doi:10.1016/0033-5894(91)90064-C.

Sprovieri, M., N. Sabatino, N. Pelosi, S. J. Batenburg, R. Coccioni, M. Iavarone, and S. Mazzola (2013), Late Cretaceous orbitally-paced carbon isotope stratigraphy from the Bottaccione Gorge (Italy), Palaeogeogr., Palaeoclimatol. Palaeoecol., 379–380, 1–94, doi:10.1016/j.palaeo.2013.04.006.

Stoll, H. and Schrag, D. (2000), High-resolution stable isotope records from the Upper Cretaceous rocks of Italy and Spain: Glacial episodes in a greenhouse planet? Geol. Soc. Am. Bull., 112, 308–319.

Taner, M. T. (1992), Attributes revisited, technical publication. Rock solid images, Inc., Houston, TX. Retrieved from http://rocksolidimages. com/pdf/attrib_revisited.htm (updated 2003).

Thomson, D.J. (1982), Spectrum estimation and harmonic analysis: Proc. IEEE, v. 70, p. 1055–1096.

Uličný, D., Laurin, J., and Čech, S. (2009), Controls on clastic sequence geometries in a shallow- marine, transtensional basin: the Bohemian Cretaceous Basin, Czech Republic: Sedimentology, 56, 1077–1114.

Uličný, D., Jarvis, I., Gröcke, D.R., Čech, S., Laurin, J., Olde, K., Trabucho-Alexandre, J., Švábenická, L. and Pedenychouk, N. (2014), A high-resolution carbon-isotope record of the Turonian stage correlated to a siliciclastic basin fill: Implications for mid-Cretaceous sea-level change: Palaeogeography Palaeoclimatology Palaeoecology, 405, 42–58.

Voigt, S., J. Erbacher, J. Mutterlose, W. Weiss, T. Westerhold, F. Wiese, M. Wilmsen, T. Wonik (2008), The Cenomanian–Turonian of the Wunstorf section (North Germany): global stratigraphic reference section and new orbital time scale for Oceanic Anoxic Event 2, Newslett. Stratigr., 43, 65–89.

Voigt, S., Aurag, A., Leis, F. and Kaplan, U. (2007), Late Cenomanian to Middle Turonian high-resolution carbon isotope stratigraphy: new data from the Mu!nsterland Cretaceous Basin, Germany. Earth Planet. Sci. Lett., 253, 196.

Waltham, D. (2015), Milankovitch period uncertainties and their impact on cyclostratigraphy, J. Sediment. Res., 85, 990-998, doi:10.2110/jsr.2015.66

Wendler, I. (2013), A critical evaluation of carbon isotope stratigraphy and biostratigraphic implications for Late Cretaceous global correlation, Earth Sci. Rev., 126, 116-146, doi:10.1016/j.earscirev.2013.08.003.

Wendler, J. E., S. R. Meyers, I. Wendler, and J. Kuss (2014), A million-year-scale astronomical control on Late Cretaceous sea-level. Newsl. Stratigr., 47, 1-19, doi:10.1127/0078-0421/2014/0038.

Wu, H., Zhang, S., Jiang, G., Hinnov, L., Yang, T., Li, H., Wan, X., Wang, C. (2013), Astrochronology of the Early Turonian–Early Campanian terrestrial succession in the Songliao Basin, northeastern China and its implications for long-period behavior of the Solar System. Palaeogeogr. Palaeoclimatol. Palaeoecol., 385, 55–70.

Zeebe, R.E. (2017), Numerical Solutions for the Orbital Motion of the Solar System over the Past 100 Myr: Limits and New Results, The Astronomical Journal, 154, no. 5, doi: 10.3847/1538-3881/aa8cce

Zeebe, R.E., and Lourens, L.J. (2019), Solar System chaos and the Paleocene–Eocene boundary age constrained by geology and astronomy. Science, 365 (6456), 926-929, doi:10.1126/science.aax0612.

Zeebe, R. E., Westerhold, T., Littler, K., & Zachos, J. C. (2017), Orbital forcing of the Paleocene and Eocene carbon cycle. Paleoceanography, 32, 440–465. https://doi.org/10.1002/2016PA003054

Zeeden, C., Meyers, S.R., Lourens, L.J., Hilgen, F.J. (2015), Testing astronomically tuned age models, Paleoceanography, 30, 369-383, doi: 10.1002/2014PA002762.

FIGURE CAPTIONS

Table 1. Comparison of published age estimates for the Early Turonian. CIE = carbon-isotope excursion; n.d. = not defined explicitly.

Table 2. Age calibration of chronostratigraphic boundaries and carbon-isotope excursions (CIE) in reference boreholes. C.w. = *Collignoniceras woollgari*. CI = confidence interval.

Figure 1. Overview of chronology (GTS2012; Gradstein et al. 2012) and carbon-isotope stratigraphy of the study interval. Major carbon-isotope anomalies (CIEs) are highlighted by blue shading (positive anomalies) and yellow shading (negative anomalies). The Lower/Middle Turonian boundary is defined by the first occurrence (FO) of *Collignoniceras woollgari*, which is penecontemporaneous with the Lulworth CIE (Jarvis et al. 2006). **(a)** English Chalk reference curve; modified after Jarvis et al. (2006); age calibration after Pearce et al. (2020). **(b)** Borehole Bch-1, Bohemian Cretaceous Basin (Uličný et al. 2014; Jarvis et al. 2015). **(c)** USGS #1 Portland core, Western Interior Basin; lower part (black) after Sageman et al. 2006 ("min option" in their fig. 1); upper part (blue) after Joo and Sageman (2014). **(d)** Wunstorf core, age calibrated (floating astrochronology after Voigt et al. 2008). **(e)** Contessa section plotted in the depth domain (Stoll and Schrag 2000). **(f)** Eccentricity maxima interpreted by Batenburg et al. (2016).

Figure 2. Paleogeographic context. **(a)** Plate tectonic reconstruction after Hay et al. (1999). Land/sea distribution is simplified after the PALEOMAP Project, C.R. Scotese (www.scotese.com). BCB = the Bohemian Cretaceous Basin. **(b)** Detail of the study area (modified after Uličný et al. 2009, 2014) plotted in the present-day coordinate system.

Figure 3. Reference boreholes and data discussed in this study. Numbers 1a through 46 denote correlation markers (see Figs. S1-S6 for a detailed correlation and Figs. S7-S8 for lithology). Carbon isotope excursions in the Lower Turonian are labelled "se-20", "be-20", etc., where "se" and "be" refer to the location (Sedlec and Beřkovice, respectively). Grey shading highlights the Oceanic Anoxic Event II (OAE II). GR = gamma ray, RES = resistivity, XNN = neutron-neutron log. Blue shading marks the correlation uncertainty of the Cenomanian-Turonian and Lower-Middle Turonian boundaries (Figs. S1-S6 and S13). Type A cycles = carbonate-dominated lithofacies; Type B = siliciclastic-dominated lithofacies (Figs. S7 and S8). Lithostratigraphy after Čech et al. (1980). Genetic sequences after Uličný et al. (2009). Wavy line = omission surface.

Figure 4. Spectral estimates, borehole J-719670. **(a)** Resistivity log (RES). Labels 1a through 45 denote correlation markers most of which correspond to maxima in the S_4 signal. **(b)** MTM (3 2π) amplitude estimate for the common logarithm of RES obtained with a 7-m moving window (EHA). F-test significance estimates are presented in Fig. S9. Potential signals are labelled S_1 through S_4. Interference patterns (IP) are highlighted by arches ")". Note that the amplitude and F-test maxima corresponding to the S_4 signal migrate towards lower frequencies

paralleling an upward increase in sand contents and a large-scale progradational pattern in the coeval siliciclastic system (Fig. S1). The EHA pattern resembles a reciprocal function of signal wavelength, consistent with a linear increase in sedimentation rate. **(c)** Resistivity log and EHA amplitude after removal of the linear trend. Intervals of constructive interference of S_{4a} and S_{4b} signals (x) delineate ~100-kyr eccentricity maxima. **(d)** MTM and ASM results for the interval 380-418m. The ASM analysis is based on all F-test maxima exceeding the 0.90 level between frequencies 0 and 5 cycle/m. Ho/SL = null-hypothesis significance level. Sedimentation rates constrained by GTS2012 are shown by ochre shading. Blue lines and symbols indicate the best fit to the astronomical terms of long eccentricity (E_1; 405 kyr period), short eccentricity ($E_{2,3}$; 127 and 97 kyr periods), obliquity ($O_{1,2}$; 49 and 39 kyr periods) and precession ($P_{1\text{-}4}$; 23 - 19 kyr periods; Tab. S2a).

Figure 5. Correlation of astronomical signals. **(a, b)** Astronomical signatures in boreholes J-719670 and J-650704; setup as in Fig. 4. Intervals of constructive interference of the S_{4a} and S_{4b} signals (x) delineate ~100-kyr eccentricity maxima. Series of strong interference patterns (IP) in the EHA plot mark 405-kyr maxima (ochre shading) superimposed upon a maximum in ~2.4-Myr modulation (cf. Fig. 5c). Note that the fidelity of S_4 envelopes and polarity of S_1 (405-kyr) signals would remain uncertain without IP (cf. Laurin et al. 2016). **(c)** Comparison with the astronomical solution La2010d (Laskar et al. 2011a); the nearest interval compatible with eccentricity phasing in the study interval. Filter setup (Taner, roll-off rate 4×10^4): J-719670, S_4 = 1.00±0.30 cycle/m, S_2 = 0.20±0.05 cycle/m, S_1 = 0.05±0.01 cycle/m; J-650704, S_4 = 1.15±0.35 cycle/m, S_2

= 0.23±0.05 cycle/m, S_1 = 0.05±0.01 cycle/m; La2010d, prec. = 50±15 cycle/Myr, short ecc. = 10±3 cycle/Myr, long ecc. = 2.47±0.5 cycle/Myr.

Figure 6. Interpretation of astronomical signatures, borehole 4523-A. **(a)** Carbon-isotope data, greyscale and filtered signals. Filter setup (Taner, roll-off rate 4×10^4): S_4 = 1.00±0.30 cycle/m, S_2 = 0.23±0.05 cycle/m. **(b)** EHA spectral estimate for greyscale data; dashed lines denote the expected trace of the S_4 (precessional) signal inferred from correlation to borehole J-719670 (5-m moving average). **(c)** MTM and ASM estimates for greyscale data, interval 190-203 m. See Tables S2a and S2b for ASM setup. Sedimentation rates constrained by GTS2012 are shown by ochre shading.

Figure 7. Eccentricity framework constraining the tuning target (see also Figs. S14 and S15). **(a-d)** Filtered precessional and eccentricity signals in reference boreholes. Maxima in short-eccentricity cycles (~100 kyr; labelled ecc1 through ecc11) are inferred using a combination of bandpassed S_2 and amplitude envelopes of the precessional signal (S_4): in the middle and upper parts of the succession that exhibit distinct precessional modulations (Fig. 5), the ~100-kyr maxima are based primarily on amplitude envelopes of the S_4 signal in borehole J-719670; the lower part of the succession exhibits less stable precessional signals; ~100-kyr maxima ecc1-ecc3 are therefore placed at maxima in the S_2 bandpass (see text). Long-eccentricity, 405-kyr, maxima (ochre shading) are placed at intervals with strong precessional interference patterns (Figs. 4 and 5). **(e)** Bundling ratios of precessional (P) vs. short-eccentricity (E) signals in the study interval. **(f)** Correlation to the nearest compatible segments of the

astronomical solutions La2010d (Laskar et al. 2011a) and La2004 (Laskar et al. 2004). Filter setup (Taner, roll-off rate 4×10^4): Bch-1, S_2 = 0.15±0.04 cycle/m; 4523-A, S_4 = 1.00±0.30 cycle/m, S_2 = 0.23±0.05 cycle/m, S_1 = 0.05±0.01 cycle/m; J-719670, S_4 = 1.00±0.30 cycle/m, S_2 = 0.20±0.05 cycle/m, S_1 = 0.05±0.01 cycle/m; J-650704, S_4 = 1.15±0.35 cycle/m, S_2 = 0.23±0.05 cycle/m, S_1 = 0.05±0.01 cycle/m; La2004 and La2010d, prec. = 50±15 cycle/Myr, short ecc. = 10±3 cycle/Myr, long ecc. = 2.47±0.5 cycle/Myr.

Figure 8. Updated chronology and eccentricity phasing for the Early Turonian. **(a)** Chronology; duration of the Early Turonian is estimated as 885 ±46 kyr (Tab. 2); the floating astrochronology is anchored to the GTS2012 age of the C/T bondary (93.9 ±0.15 Myr ago). Duration of the Cenomanian part of OAE II (shaded) is based on Sageman et al. (2006) and Ma et al. (2014); Fig. S13. **(b)** The nearest segment of the astronomical solution La2010d (Laskar et al. 2011a) whose eccentricity phasing is compatible with eccentricity signatures in the study interval (Figs. 4, 5 and 7). Filter setup as in Figure 7. Well-preserved modulation in the middle and upper parts of the study interval suggests that these intervals overlap with a ~2.4-Myr eccentricity maximum. If so, then OAE II coincides with a node in the 2.4-Myr cycle, in agreement with previous results (Batenburg et al. 2016; Laurin et al. 2016). **(c)** Timing of 405-kyr eccentricity maxima (ochre shading) and minima inferred in this study. Comparison with eccentricity phasing at Furlo (Italy) is shown at the bottom; IRM = Isothermal Remanent Magnetization; black = sum of eccentricity components; red = 405 kyr (Laurin et al. 2016). **(d)** EHA estimate for age-calibrated $\delta^{13}C_{org}$, borehole 4523-A. **(e)** Age-calibrated carbon-isotope curves. The Early Turonian interval of 4523-A

is calibrated in high-resolution as described in sections 4.4 and 4.5. A linear sedimentation rate of 1.55 cm/kyr is applied to the Cenomanian segment of 4523-A, beneath marker 1a (grey part of $\delta^{13}C$ curve; Fig. S13). Local isotope excursions are indicated ("se-6", etc.). Age calibration of the Wunstorf record is adopted from Voigt et al. (2008). English Chalk (Jarvis et al. 2006; Pearce et al. 2020) and Portland (black: Sageman et al. 2006; blue: Joo and Sageman 2014) records are recalibrated in the time domain by linearly adjusting the duration of the Early Turonian. Abbreviations: *I.c. = Inoceramus cuvieri, C.w. = Collignoniceras woollgari, M.n. = Mammites nodosoides, M.pu. = Mytiloides puebloensis, W.d. = Watinoceras devonense, M.g. = Metoicoceras geslinianum.*

Reference	Location	Duration of Early Turonian [Myr]	Un-certainty [± Myr]	Pros	Cons
Sageman et al. (2006); Meyers et al. (2012a)	Portland	0.785	n.d.	Robust astronomical signature	Short-eccentricity tuning target, monochromatic (95 kyr); modulation of the tuning target not considered
Voigt et al. (2008)	Wunstorf	0.84	n.d.	Precession-scale resolution; robust astronomical signature	Precession-paced chronology does not reach the top of Early Turonian; modulation of the tuning target not considered
Gradstein et al. 2012 (GTS 2012)		1.0	n.d.		Meyers et al. (2012a) misquoted [1]); Voigt et al. (2008) not considered
Sprovieri et al. (2013)	Bottaccione	0.6-0.8	n.d.	Well-defined 405-kyr signature	No ammonite zonation; reduced resolution near C/T boundary
Eldrett et al. (2015; their fig. 11)	Iona	1.14	n.d.	High-resolution astronomical signature	No ammonite zonation; Early/Middle Turonian boundary placed deep into a major positive CIE (runup to Round Down CIE)
Batenburg et al. (2016)	Contessa	0.6-1.2	n.d.	Well-defined eccentricity signature	No ammonite zonation; C/T boundary controversial (cf. Wendler 2013; Fig. 1)
This study	Bohemian Cretaceous Basin	0.885	0.046	Precession-scale resolution; robust eccentricity phasing; modulation of the tuning target included in uncertainty	Biostratigraphy correlated from adjacent boreholes (correlation uncertainty acknowledged in the uncertainty range)

[1]) *The duration of W. devonense Zone is given as 0.35 Myr with reference to Meyers et al. (2012a); Meyers et al. (2012a), however, indicate ~0.2 Myr (two short-eccentricity cycles; their figure 1).*

Table 1. Comparison of published age estimates for the Early Turonian. CIE = carbon-isotope excursion; n.d. = not defined explicitly.

Stratigraphic level	J-719670			J-650704			4523-A		
	depth [m]	mean floating age [kyr]	uncert. 95% CI [kyr]	depth [m]	mean floating age [kyr]	uncert. 95% CI [kyr]	depth [m]	mean floating age [kyr]	uncert. 95% CI [kyr]
base Middle Turonian (FO *C.w.*), upper limit	360.7	902	+20/-16	384.9	903	+14/-14	144.50	915	+22/-29
Lulworth CIE ($\delta^{13}C$ trough)							146.75	890	+27/-22
base Middle Turonian (FO *C.w.*), lower limit	364.5	865	+19/-22	391.0	860	+19/-22	148.50	872	+21/-23
CIE "se-20" peak							178.75	521	+21/-19
CIE "se-10" peak							185.75	315	+20/-18
CIE "se-6" peak							191.25	203	+15/-12
CIE "se-e2o" peak							196.25	79	+16/-15
C/T boundary, upper limit	423.6	11	+17/-7	446.8	11	+22/-7	198.75	17	+16/-9
C/T boundary, lower limit	424.5	-13	+3/-4	447.5	-15	+3/-3	199.75	-9	+3/-2
Onset of OAE II recovery							199.75	-9	+3/-2
Duration of Early Turonian		**885**	**±46 [1])**		884	±49 [1])		890	±53 [1])

[1]) Combined uncertainty, calculated using summation in quadrature
C.w. = *Collignoniceras woollgari*
CI = confidence interval

Table 2. Age calibration of chronostratigraphic boundaries and carbon-isotope excursions (CIE) in reference boreholes.

Figure 1.

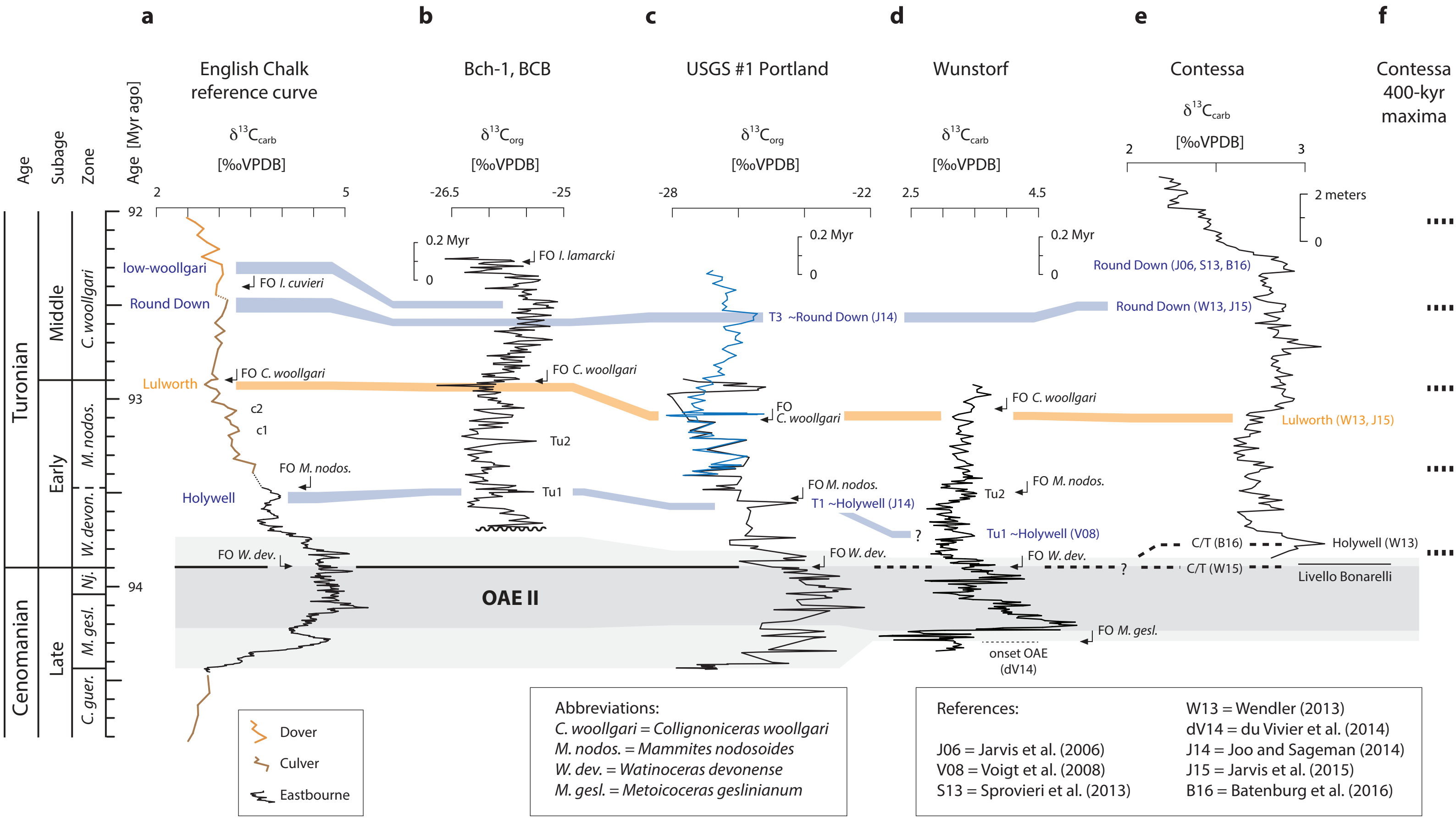
a
b
c
d
e
f
English Chalk reference curve
Bch-1, BCB
USGS #1 Portland
Wunstorf
Contessa
Contessa 400-kyr maxima
Age
Subage
Zone
Age [Myr ago]
δ13Ccarb [‰VPDB]
δ13Corg [‰VPDB]
δ13Corg [‰VPDB]
δ13Ccarb [‰VPDB]
δ13Ccarb [‰VPDB]
Turonian
Middle
Early
Cenomanian
Late
C. woollgari
M. nodos.
W. devon.
Nj.
M. gesl.
C. guer.
92
93
94
2
5
-26.5
-25
-28
-22
2.5
4.5
2
3
2 meters
0
0.2 Myr
0
low-woollgari
Round Down
Lulworth
Holywell
FO I. cuvieri
FO C. woollgari
FO M. nodos.
FO W. dev.
c2
c1
FO I. lamarcki
Tu2
Tu1
T3 ~Round Down (J14)
FO C. woollgari
T1 ~Holywell (J14)
Tu1 ~Holywell (V08)
?
Round Down (J06, S13, B16)
Round Down (W13, J15)
Lulworth (W13, J15)
Holywell (W13)
C/T (B16)
C/T (W15)
Livello Bonarelli
FO M. gesl.
onset OAE (dV14)
OAE II
Dover
Culver
Eastbourne
Abbreviations:
C. woollgari = Collignoniceras woollgari
M. nodos. = Mammites nodosoides
W. dev. = Watinoceras devonense
M. gesl. = Metoicoceras geslinianum
References:
J06 = Jarvis et al. (2006)
V08 = Voigt et al. (2008)
S13 = Sprovieri et al. (2013)
W13 = Wendler (2013)
dV14 = du Vivier et al. (2014)
J14 = Joo and Sageman (2014)
J15 = Jarvis et al. (2015)
B16 = Batenburg et al. (2016)

Figure 2.

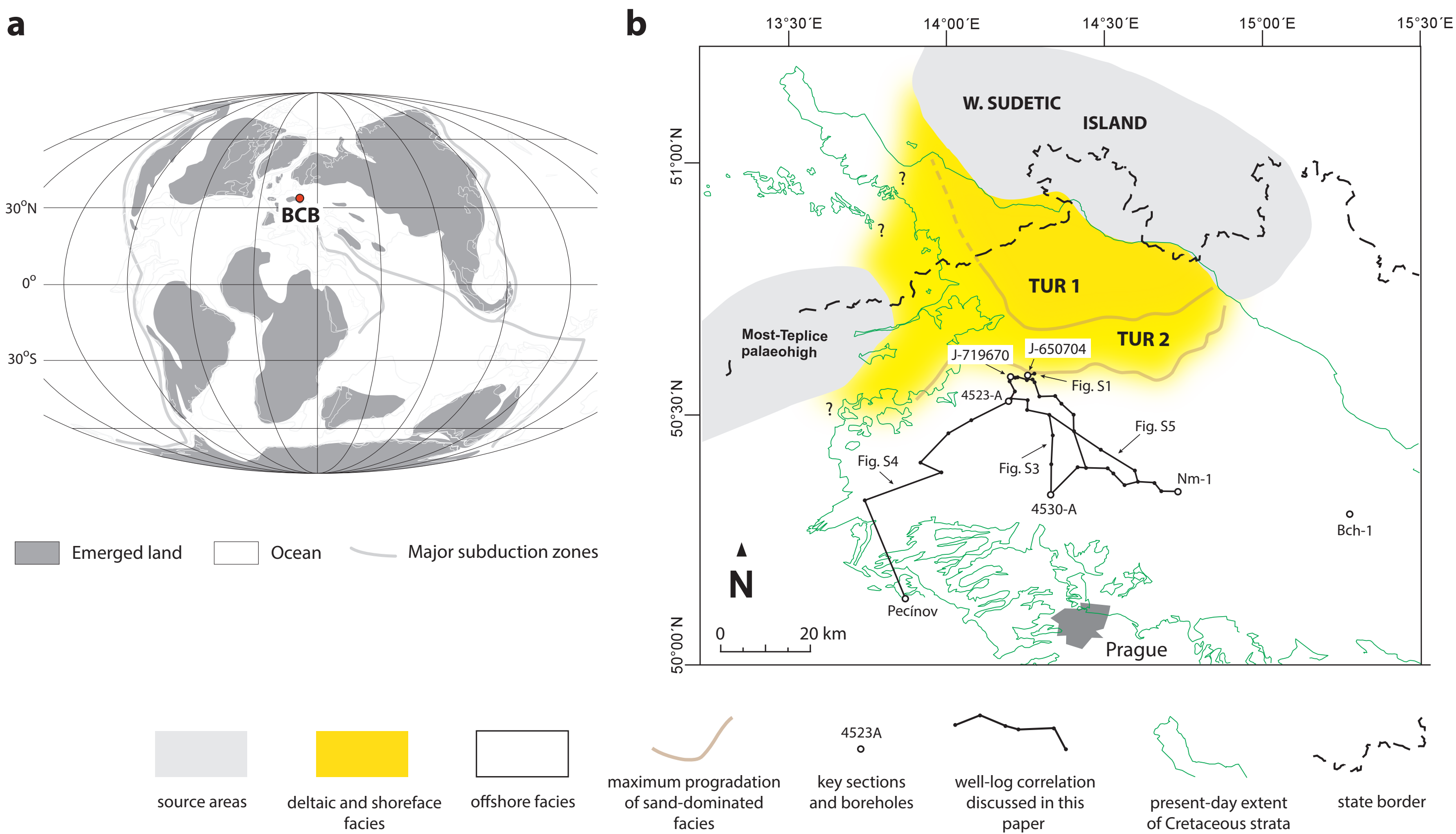

a
30°N
0°
30°S
BCB
Emerged land
Ocean
Major subduction zones
b
13°30´E
14°00´E
14°30´E
15°00´E
15°30´E
51°00´N
50°30´N
50°00´N
W. SUDETIC
ISLAND
TUR 1
TUR 2
Most-Teplice
palaeohigh
J-719670
J-650704
Fig. S1
4523-A
Fig. S5
Fig. S4
Fig. S3
Nm-1
4530-A
Bch-1
N
Pecínov
0
20 km
Prague
source areas
deltaic and shoreface facies
offshore facies
maximum progradation of sand-dominated facies
4523A
key sections and boreholes
well-log correlation discussed in this paper
present-day extent of Cretaceous strata
state border

Figure 3.

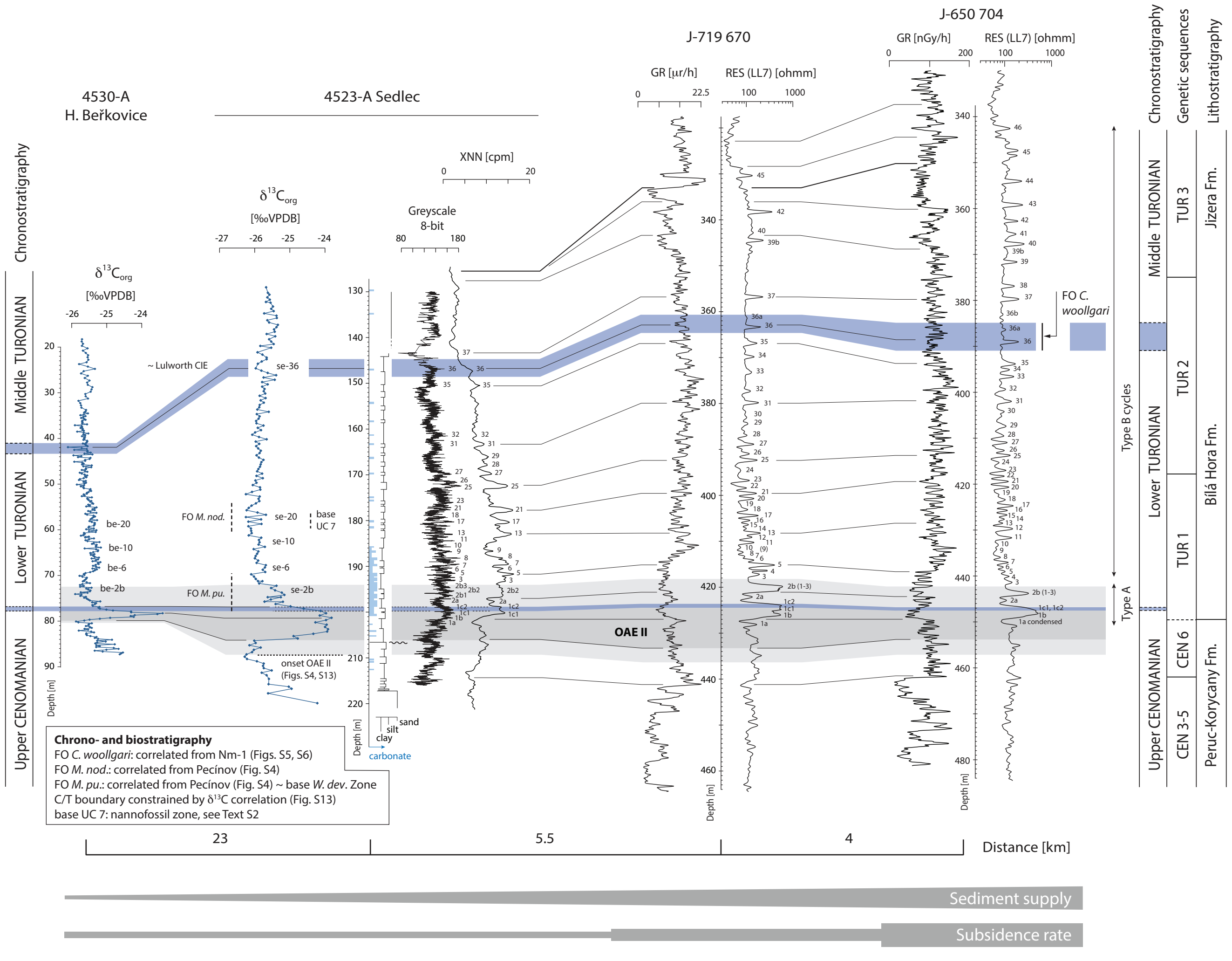

4530-A
H. Beřkovice
4523-A Sedlec
J-719 670
J-650 704
Chronostratigraphy
Genetic sequences
Lithostratigraphy
δ13Corg [‰VPDB]
Greyscale 8-bit
XNN [cpm]
GR [μr/h]
RES (LL7) [ohmm]
GR [nGy/h]
Depth [m]
Middle TURONIAN
Lower TURONIAN
Upper CENOMANIAN
TUR 3
TUR 2
TUR 1
CEN 6
CEN 3-5
Jizera Fm.
Bílá Hora Fm.
Peruc-Korycany Fm.
~ Lulworth CIE
FO M. nod.
FO M. pu.
base UC 7
onset OAE II (Figs. S4, S13)
OAE II
FO C. woollgari
Type B cycles
Type A
sand
silt
clay
carbonate
Chrono- and biostratigraphy
FO C. woollgari: correlated from Nm-1 (Figs. S5, S6)
FO M. nod.: correlated from Pecínov (Fig. S4)
FO M. pu.: correlated from Pecínov (Fig. S4) ~ base W. dev. Zone
C/T boundary constrained by δ13C correlation (Fig. S13)
base UC 7: nannofossil zone, see Text S2
23
5.5
4
Distance [km]
Sediment supply
Subsidence rate

Figure 4.

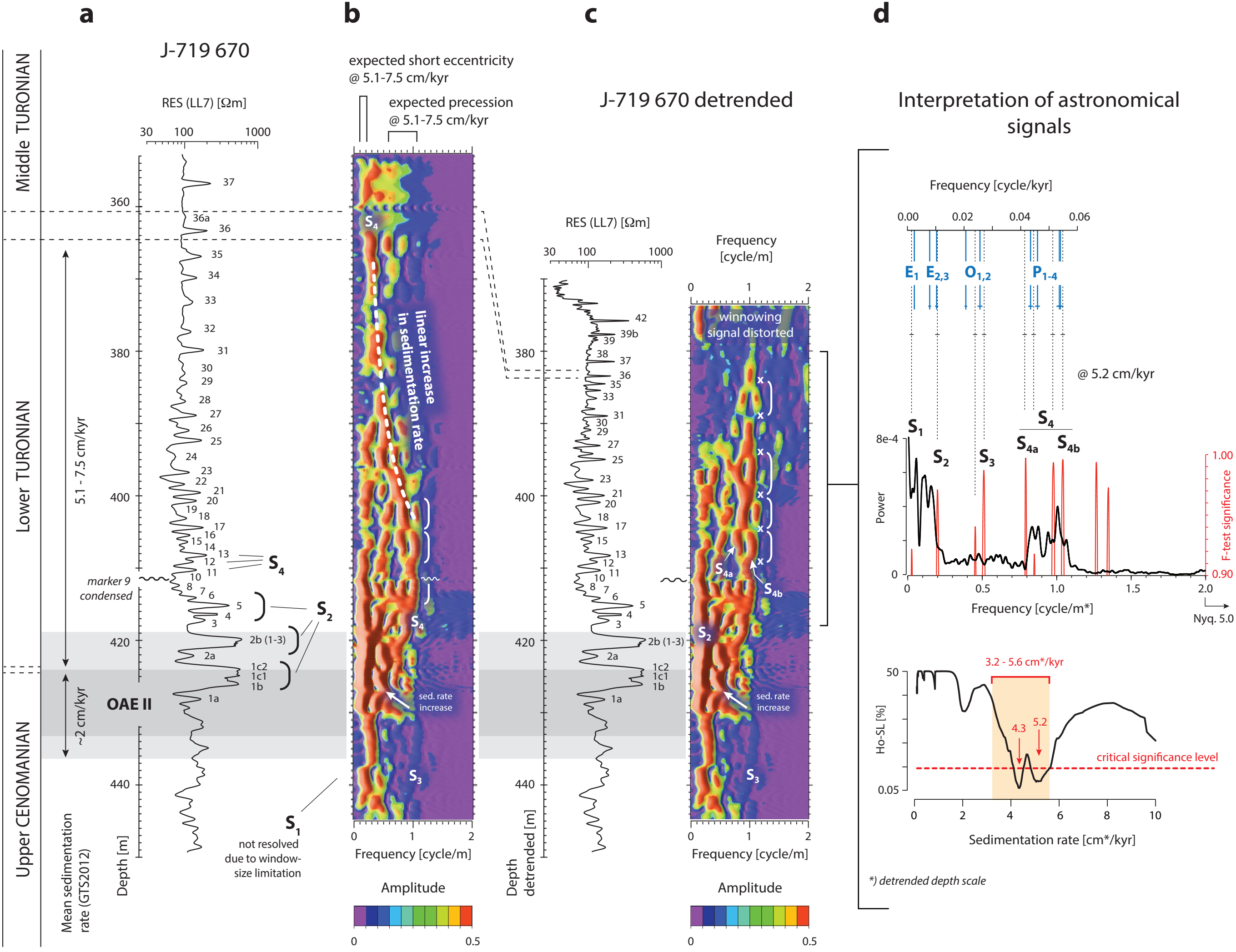
a
b
c
d
J-719 670
RES (LL7) [Ωm]
Middle TURONIAN
Lower TURONIAN
Upper CENOMANIAN
5.1 - 7.5 cm/kyr
~2 cm/kyr
OAE II
marker 9 condensed
Mean sedimentation rate (GTS2012)
Depth [m]
S4
S2
S1
not resolved due to window-size limitation
expected short eccentricity @ 5.1-7.5 cm/kyr
expected precession @ 5.1-7.5 cm/kyr
linear increase in sedimentation rate
sed. rate increase
S3
Frequency [cycle/m]
Amplitude
J-719 670 detrended
Depth detrended [m]
winnowing signal distorted
S4a
S4b
Interpretation of astronomical signals
Frequency [cycle/kyr]
E1
E2,3
O1,2
P1-4
@ 5.2 cm/kyr
Power
F-test significance
Frequency [cycle/m*]
Nyq. 5.0
3.2 - 5.6 cm*/kyr
Ho-SL [%]
critical significance level
Sedimentation rate [cm*/kyr]
*) detrended depth scale

Figure 5.

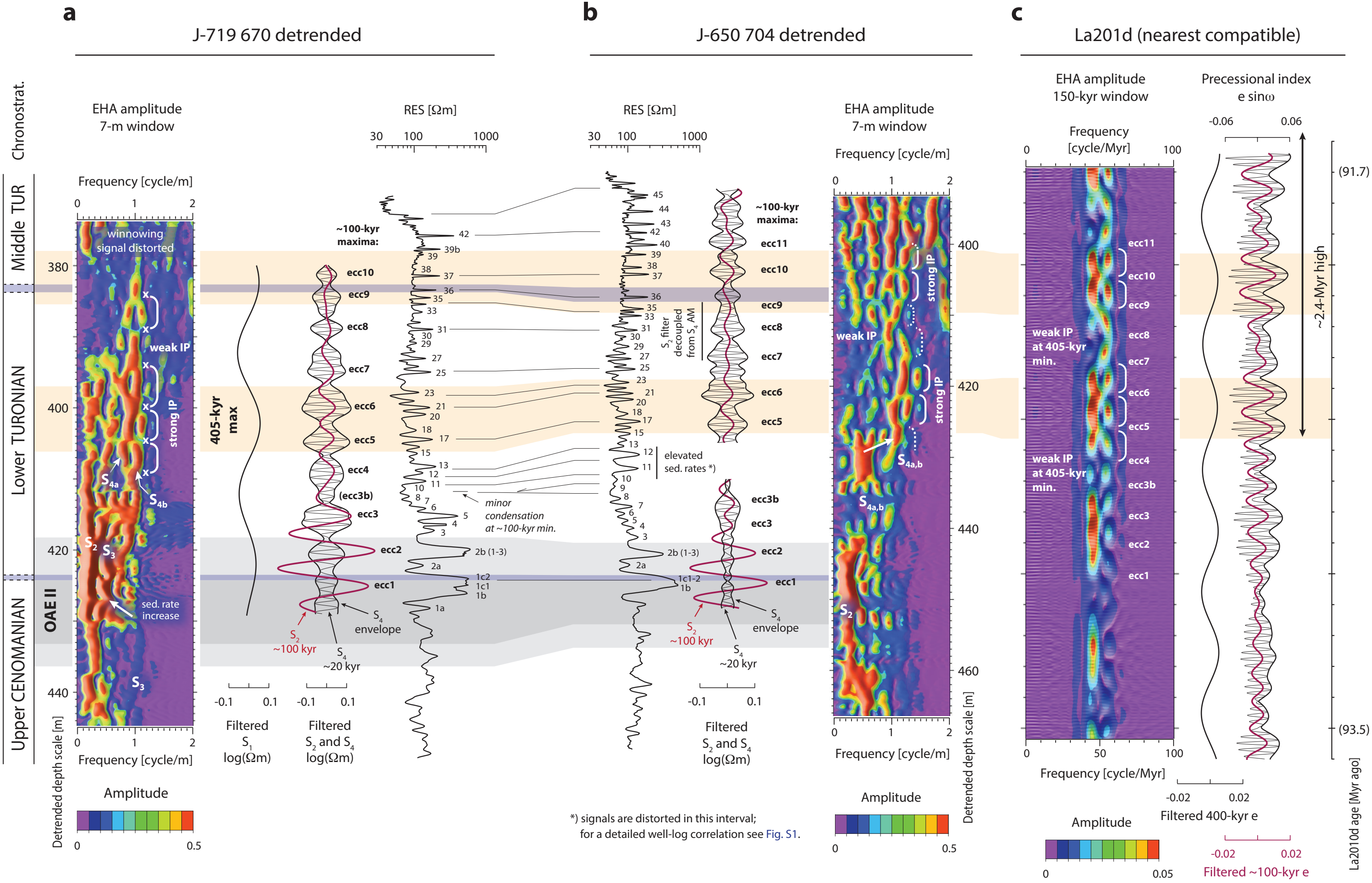
a
J-719 670 detrended
b
J-650 704 detrended
c
La201d (nearest compatible)
Chronostrat.
Middle TUR
Lower TURONIAN
Upper CENOMANIAN
OAE II
EHA amplitude
7-m window
Frequency [cycle/m]
winnowing signal distorted
weak IP
strong IP
sed. rate increase
405-kyr max
RES [Ωm]
~100-kyr maxima:
minor condensation at ~100-kyr min.
elevated sed. rates *)
S4 envelope
S2 ~100 kyr
S4 ~20 kyr
Filtered S1 log(Ωm)
Filtered S2 and S4 log(Ωm)
Detrended depth scale [m]
Amplitude
S2 filter decoupled from S4 AM
weak IP at 405-kyr min.
EHA amplitude
150-kyr window
Frequency [cycle/Myr]
Precessional index
e sinω
~2.4-Myr high
Filtered 400-kyr e
Filtered ~100-kyr e
La2010d age [Myr ago]
*) signals are distorted in this interval; for a detailed well-log correlation see Fig. S1.

Figure 6.

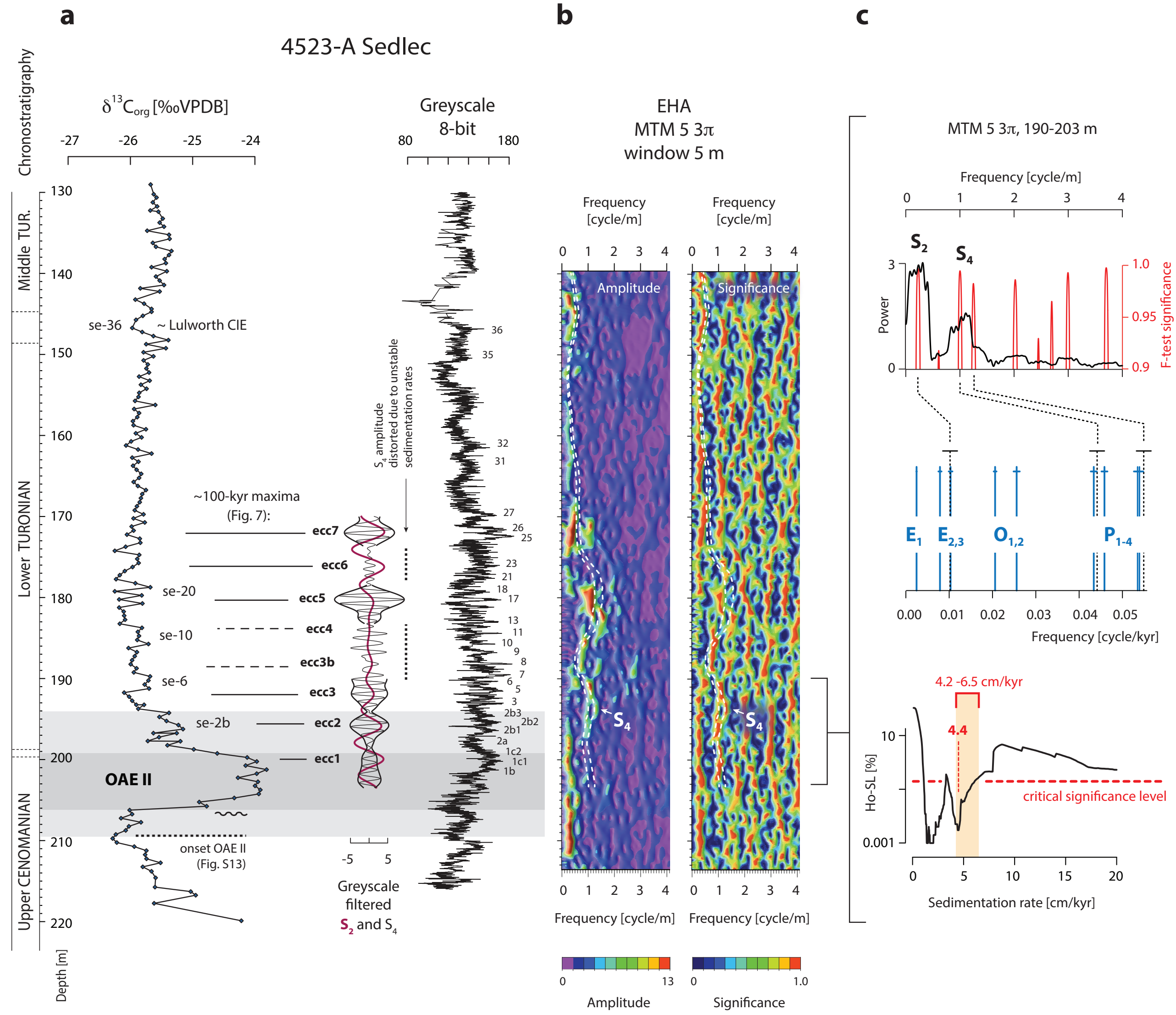

a
b
c
4523-A Sedlec
Chronostratigraphy
δ13Corg [‰VPDB]
Greyscale 8-bit
Middle TUR.
Lower TURONIAN
Upper CENOMANIAN
Depth [m]
se-36
~ Lulworth CIE
~100-kyr maxima (Fig. 7):
ecc7
ecc6
ecc5
ecc4
ecc3b
ecc3
ecc2
ecc1
se-20
se-10
se-6
se-2b
OAE II
onset OAE II (Fig. S13)
S4 amplitude distorted due to unstable sedimentation rates
Greyscale filtered S2 and S4
EHA
MTM 5 3π
window 5 m
Frequency [cycle/m]
Amplitude
Significance
MTM 5 3π, 190-203 m
Power
F-test significance
E1
E2,3
O1,2
P1-4
Frequency [cycle/kyr]
4.2 -6.5 cm/kyr
4.4
Ho-SL [%]
critical significance level
Sedimentation rate [cm/kyr]

Figure 7.

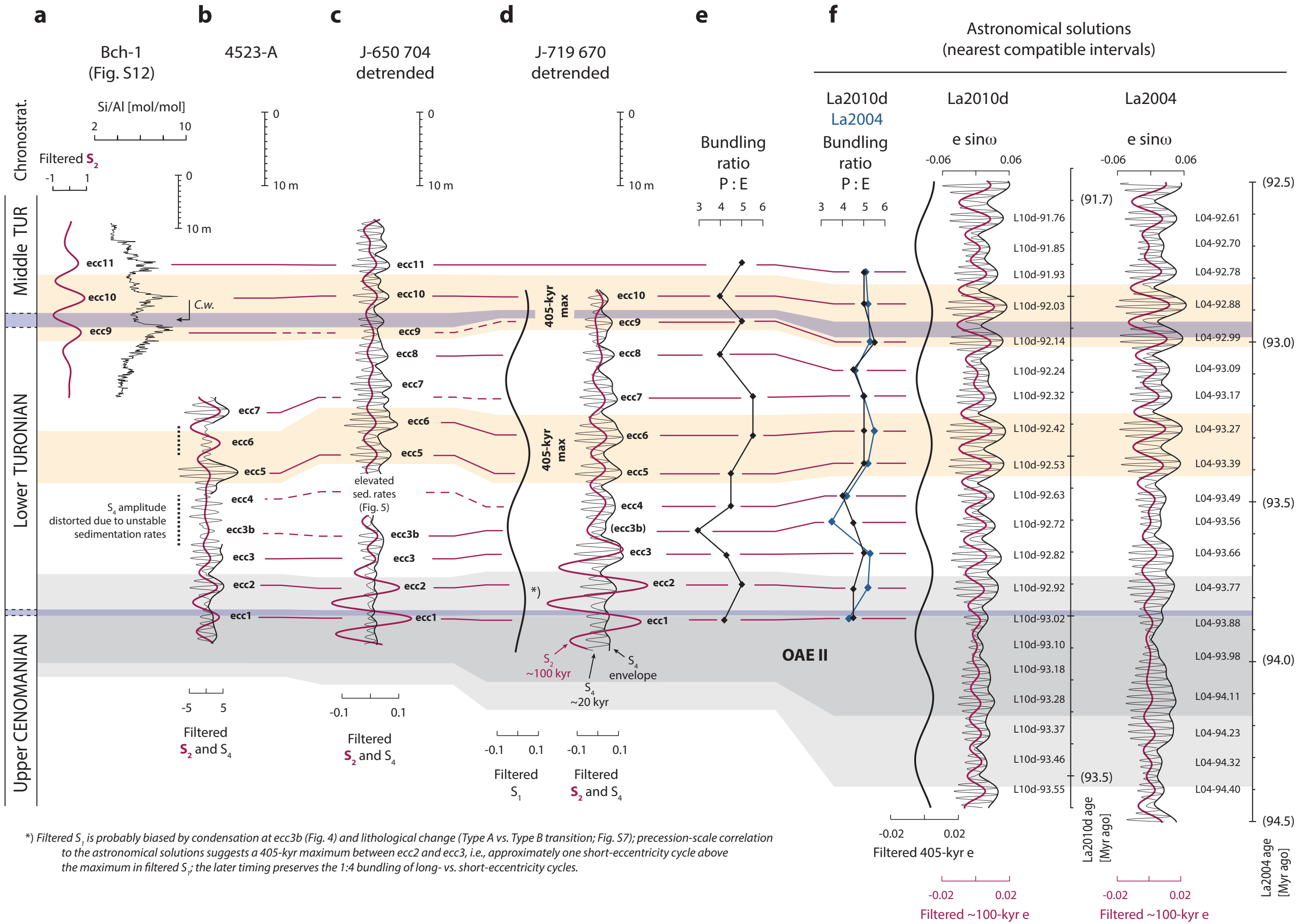

*) Filtered S_1 is probably biased by condensation at ecc3b (Fig. 4) and lithological change (Type A vs. Type B transition; Fig. S7); precession-scale correlation to the astronomical solutions suggests a 405-kyr maximum between ecc2 and ecc3, i.e., approximately one short-eccentricity cycle above the maximum in filtered S_1; the later timing preserves the 1:4 bundling of long- vs. short-eccentricity cycles.

Figure 8.

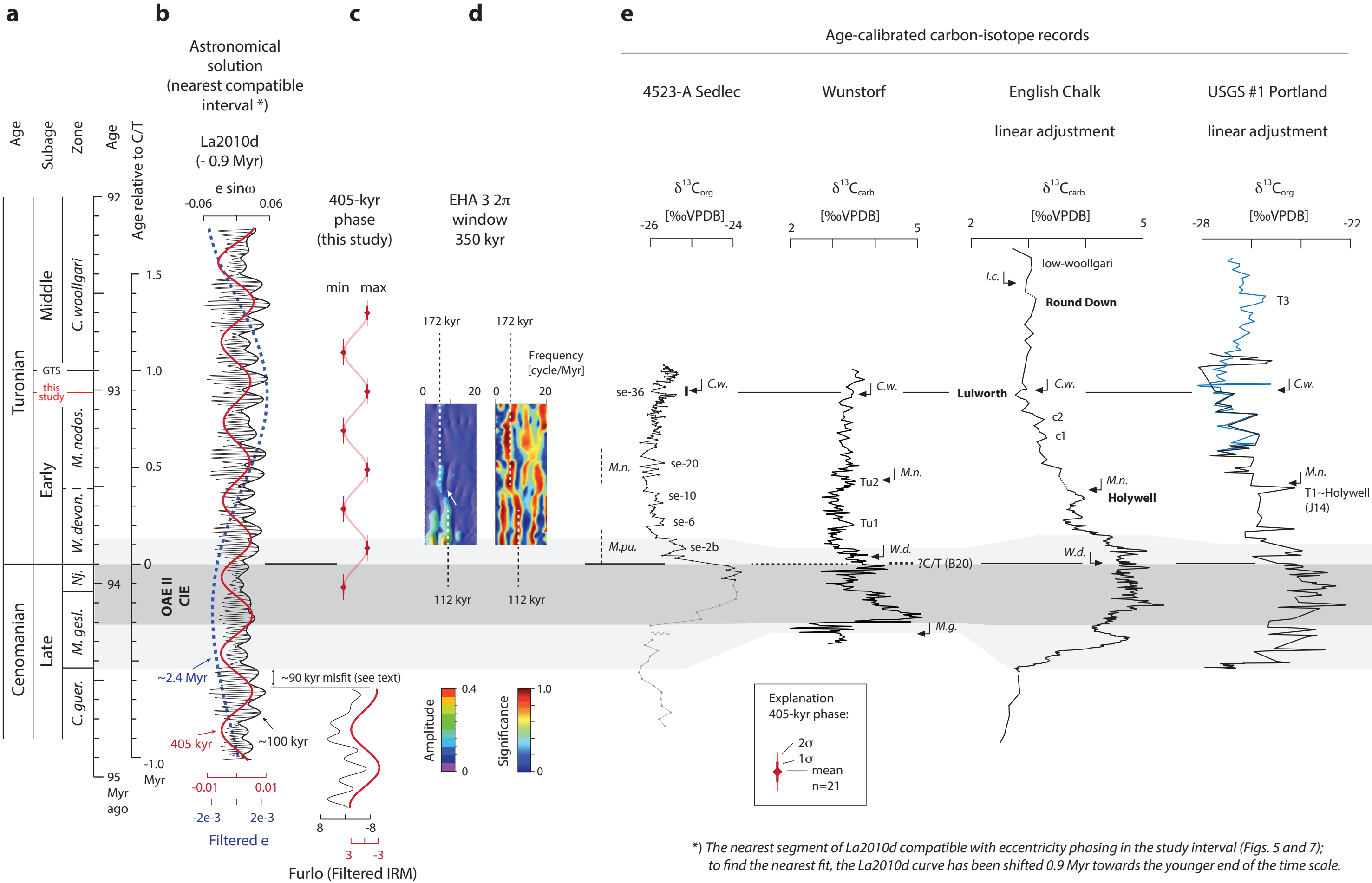

*) The nearest segment of La2010d compatible with eccentricity phasing in the study interval (Figs. 5 and 7); to find the nearest fit, the La2010d curve has been shifted 0.9 Myr towards the younger end of the time scale.